



Masterthesis

# Non-invasive analysis of fire gilded layers

Faculty of Mathematics and Natural Sciences  
of the University of Cologne

Study course M. Sc. Chemistry

Submitted by

Raphael Margreiter

Cologne, November 2019

# Eidesstattliche Erklärung

Hiermit versichere ich, Raphael Margreiter, an Eides statt, dass ich die vorliegende Arbeit mit dem Thema

**"Non-invasive analysis of fire gilded layers"**

selbstständig und ohne die Benutzung anderer als der angegebenen Hilfsmittel angefertigt habe.

Alle Stellen, die wörtlich oder sinngemäß aus veröffentlichten oder nicht veröffentlichten Schriften entnommen wurden, sind als solche kenntlich gemacht. Die Arbeit ist in gleicher oder ähnlicher Form oder auszugsweise im Rahmen einer anderen Prüfung noch nicht vorgelegt worden.

Ich versichere, dass die eingereichte elektronische Fassung der eingereichten Druckfassung vollständig entspricht.

---

(Ort, Datum)

---

(Unterschrift)

# Contents

<b>Eidesstattliche Erklärung</b>	<b>I</b>
<b>List of Figures</b>	<b>III</b>
<b>List of Tables</b>	<b>IV</b>
<b>List of Acronyms &amp; Symbols</b>	<b>V</b>
<b>1 Introduction</b>	<b>1</b>
1.1 Gilding . . . . .	2
1.2 Motivation & Aim of this Work . . . . .	3
<b>2 Methods</b>	<b>6</b>
2.1 X-Ray Fluorescence Analysis . . . . .	6
2.1.1 XMI-MSIM . . . . .	9
2.1.2 BESSY II . . . . .	9
2.1.2.1 BAMline . . . . .	10
2.2 Particle-Induced X-ray Emission . . . . .	13
<b>3 Experimental</b>	<b>14</b>
3.1 Sample Preparation . . . . .	14
3.1.1 Additional or adjusted steps . . . . .	16
3.2 Measurements . . . . .	17
3.2.1 Spectra simulation . . . . .	17
3.2.2 Preparation analysis . . . . .	17
3.2.3 Artificial aging . . . . .	19
3.2.4 Cross section analysis . . . . .	20
3.2.5 PIXE . . . . .	24
3.3 Results . . . . .	25
3.3.1 Spectra Simulation . . . . .	25
3.3.2 Polishing & Temperature Profile . . . . .	27
3.3.3 Artificial Aging . . . . .	28
3.3.4 Cross section Analysis . . . . .	31
3.3.5 PIXE . . . . .	34
<b>4 Conclusion</b>	<b>35</b>
4.1 Summary . . . . .	35
4.2 Discussion . . . . .	36
4.3 Outlook . . . . .	37
<b>References</b>	<b>VI</b>
<b>Danksagung</b>	<b>VIII</b>
<b>Appendix</b>	<b>IX</b>

## List of Figures

1	Phasediagram of the Au-Hg-system under variable pressure. . . . .	4
2	Mercury contents of 70 different gilded silver objects from the Antikensammlung Berlin. . . . .	4
3	The schematic shows the two basic steps of XRF, the photoelectric effect and the subsequent emission of characteristic X-rays afterwards. . . . .	7
4	Basic picture of a photon-matter interaction as simulated by the Monte Carlo code. . . . .	10
5	Components of BESSY II. . . . .	11
6	Schematic picture of an undulator. . . . .	12
7	Layout of the BAMline beampath. . . . .	12
8	Picture of the measurement set up at the BAMline. . . . .	13
9	Schematic picture of the measurement set up at the BAMline with CRLs. . . . .	13
10	Picture series of the heating process during fire gilding of a copper substrate. . . . .	15
11	Unpolished fire gilded metal sheets. Copper substrate on the left, silver substrate on the right. . . . .	15
12	Pictures of fire gilding done wrong, showcasing some common difficulties and mistakes. . . . .	16
13	Fire gilded silver (left) and copper (right) sheets. The left side of each sample is polished. . . . .	18
14	Picture of a temperature gradient sample. . . . .	18
15	Exemplary picture of a series of artificial aging samples. . . . .	19
16	Exemplary picture of fire gilded copper and silver substrates embedded in an epoxyresin and subsequently cut and polished for cross section analysis. . . . .	22
17	Fire gilded silver substrates on a PIXE sample holder. . . . .	24
18	Hg content determined from simulated XRF spectra of a homogenous layer with varying thickness and a fixed Hg content of 25% . . . . .	26
19	Difference between the measured and the actual Hg content plotted against the measured Hg content for various layer thicknesses. . . . .	26
20	Analysis of the influence of polish on the measured Hg content in a sample on copper and silver. . . . .	28
21	Development of the Hg content during fire gilding on a copper substrate. . . . .	29
22	Development of the Hg content during fire gilding on a copper substrate in the context of the Au-Hg-phase diagram. . . . .	29
23	The determined Hg content in artificially aged fire gilded Ag and Cu substrates plotted against the simulated years as shown in table 14. . . . .	30
24	Absolute Hg contents of the artificially aged fire gilded Cu substrates plotted against the heating time, for different temperatures. . . . .	31
25	Plotting relative Hg contents of artificially aged Cu substrates at different temperatures against the simulated aging period. . . . .	32
26	cross section analysis of a fire gilded silver and copper substrate. The figure shows the development of the Hg content across the interface of the substrate and the gilding. . . . .	33

27	Comparison of relative Hg content distribution across the interface of fire gilded Ag substrates with different amounts of time between Au-amalgam application and Hg evaporation. . . . .	34
28	Hg contents of fire gilded and artificially aged Ag substrates as determined with XRF and PIXE. . . . .	35

## List of Tables

1	The table shows the construction of transition levels by combining the quantum numbers $n$ , $l$ , and $j$ . . . . .	8
2	Correspondence between Siegbahn and IUPAC Notations for the nomenclature of XRF-lines. . . . .	9
3	An overview over the different simulation parameters used with the XMI-MSIM Monte Carlo software. . . . .	17
4	Table of samples analysed for the influence of polish on the determined Hg content. . . . .	18
5	Table of samples prepared for temperature gradient analysis during the gilding process. . . . .	18
6	Table of preparation- and measuringparameter of the artificial aging samples for preliminary measurements. . . . .	20
7	Table of preparation- and measuringparameters of copper substrate artificial aging samples for a systematic measurement series of the effect of aging a sample at different temperatures and for different periods of time with samples made from different amalgam mixtures. . . . .	20
8	Table of preparation- and measuringparameters of artificial aging samples for a systematic measurement series of the effect of aging a sample at different temperatures and for different periods of time with samples made from the same amalgam mixture. . . . .	21
9	Measurement parameters for two cross section analysis samples (1 Cu substrate, 1 Ag substrate). . . . .	21
10	Measurement parameters for 6 Ag substrate cross section analysis samples. . . . .	22
11	Measurement parameters for 8 cross section analysis samples (4 Ag substrates, 4 Cu substrates). . . . .	23
12	Measurement parameters for the PIXE analysis of artificially aged fire gilded silver substrates. . . . .	24
13	The table lists the equations that, for a set layer thickness, can be used to determine the difference between measured and actual Hg content. . . . .	27
14	Table showing the rough timeperiode simulated with the artificial aging, if the $+10\text{ }^{\circ}\text{C} \rightarrow$ reaction rate*2 actually holds. . . . .	30

# List of Acronyms & Symbols

$I_0$  initial intensity

$I_A$  intensity after passing the matter

$\lambda_u$  spatial period

$\mu$  material and wavelength dependend attenuation coefficient

$\phi$  binding energy

$\rho$  density

$S_i$  step length

$J$  total angular momentum

$l$  angular quantum number

$m$  magnetic quantum number

$n$  principal quantum number

$s$  spin quantum number

**BAM** BundesAnstalt für Materialforschung und -prüfung

**BESSY** Berliner Elektronen-Speicherring-Gesellschaft für **SY**nchrotronstrahlung

**CRLs** Compound **R**efractive **L**enses

**d** material thickness

**DCM** Double **C**rystal **M**onochromator

**DMM** Double **M**ultilayer **M**onochromator

**HZB** Helmholtz-**Z**entrum **B**erlin für Materialien und Energie

**NAA** Neutron **A**ctivation **A**nalysis

**PIXE** Particle-Induced **X**-ray **E**mission

**PTB** Physikalisch-**T**echnische **B**undesanstalt

**XRF** **X**-**R**ay **F**luorescence analysis

# 1 Introduction

Fire gilding is a historic gilding technique, developed more than 2000 years ago. For more than 1500 years, it was the dominant gilding method in Europe until it was replaced by modern electrolytic gilding in the mid 19th century. The widespread use through the centuries makes this method particularly interesting for historical questions.

Characteristic of fire gilding is the use of mercury during the gilding process. The mercury is largely evaporated, but a certain amount stays in the golden layer. The presence of mercury in a sample is a giveaway for the use of fire gilding as gilding method.

However, recent studies revealed that the process of fire gilding might not be sufficiently understood for unambiguous identification of the technique.

Building on previous studies, this thesis works toward the development of a destruction-free unambiguous method for identification of fire gilding. For this, a more in-depth understanding of the process, and the behavior of mercury in the gilding is necessary. This is why this thesis tackles the analysis of mostly lab-made fire gilded copper and silver sheets from a variety of different angles.

The three general areas of interest presented in this thesis are:

1. The preparation of samples and the analysis of how mercury behaves during the preparation.
2. The identification of a characteristic property of fire gilded objects apart from the sheer presence of mercury. And a subsequent detection of this characteristic with a destruction-free method.
3. How different factors, such as age and layer thickness, might influence the Hg content.

This was mainly done through **X-Ray Fluorescence** analysis (XRF) performed at the BAMline of **Berliner Elektronen-Speicherring-Gesellschaft für Synchronstrahlung** (BESSY) II. These measurements were complemented with Monte Carlo simulations of XRF spectra, and an initial set of **Particle-Induced X-ray Emission** (PIXE).

Particular fields of study were the development of the Hg content during the gilding process, the influence of artificial aging and layer thickness on the detected Hg content, and analysis of cross section cuts of the gilded layers with regards to the Hg distribution.

## 1.1 Gilding

If not stated otherwise, the contents of this sections are based on publications by A. Oddy [1, 2], P.A. Lins [3], E. Darque-Ceretti [4] and A.V. Anikin [5].

The history of humanity is thoroughly intertwined with its metallurgic know-how, the technological ability to extract and process different metals. The names of different periods in humanities prehistory (Chalcolithic, Bronze Age, Iron Age) attest to this. Through the ages, technological advances facilitated civilizing, cultural, and economic changes by creating new materials and thereby opening the door for new possibilities.

Civilization changed a lot from the time humans first extracted solid copper from colorful ores in the fifth millennium BC. What has not changed however is its fascination with gold.

Gold is the noblest of naturally occurring metals, has a distinct appearance and great malleability. It usually is not present as a solid metal but in form of alloys with other metals such as copper and nickel. Due to all these factors, gold is and has been for a very long time, above all, a status symbol; used as jewelry, ornaments, currency, and investment option. In modern times, gold became more important as a valuable material in the field of electrical engineering due to its good electrical and thermic properties and its resistivity to corrosion. This, however, has little relevance to the topic at hand.

Apart from that, gold is not the most serviceable material. With a density of  $19.3 \frac{g}{cm^3}$  it is very heavy and with a Mohs hardness between 2.5 and 3, comparable to that of copper, rather soft. It is also quite expensive and hard to extract in large quantities. All this considered, gold was usually attached to the surface of pieces of other metals/materials to ennoble and decorate them, a process known as gilding.

One of the oldest gilded objects ever found, an Egyptian vase with gold decorated handles, dates back to approximately 4000 BC [4], silver nails found in Northern Syria had their heads wrapped in gold and are more than 5000 years old [6]. Both objects were gilded with a very rudimentary form of *foil gilding*: Gold is hammered into thin sheets or foils, which are then wrapped around the object in question and mechanically affixed.

The gold layer applied with this method was loose and not suited for normal wear as it could easily detach. The method evolved, however, by either applying some form of glue (e.g., egg white) or burnishing sheets of gold together. The latter method is easily possible with gold due to its non-reactivity with air or other materials, allowing overlapping gold sheets to fuse.

Around 2000 BC, the method evolved once again when methods for further purification of gold were invented in Mesopotamia. Pure gold can be hammered out into very thin gold leaves, which were then attached with an adhesive or by carving small grooves into the base material. The grooves are hammered shut to fix the foil and leaves in place. Even today, organic materials are gilded with this method.

The natural decay of the organic glues used in archeological samples usually leads to a loss of the gilding. Only small traces of gold stuck in groves and folds remain. As a side note: The term gold leaf is usually applied to gold foils so thin that they

are not able to support their weight with a thickness  $<1\mu\text{m}$ .

The next large development in the gilding process was the introduction of mercury into the process around the 3<sup>rd</sup> century BC. One of the most important roman sources for this is the *Naturalis Historia* by the Roman naturalist and author *Pliny the Elder* [7].

A long-held misconception about the way mercury was used at the time, held among other by Oddy and Vittori [8] and known as *cold mercury gilding*, that mercury was used as an adhesive applied as a thin film to the material before it was covered with layers of gold leaf and subsequently evaporated at room temperature, was based on a wrong translation of the primary source by Rackham and Warmington [9], as shown by K. Anheuser in 1999 [10].

In reality, mercury was introduced in a process now known as *fire gilding*. The method first occurred in china around the 3<sup>rd</sup> century BC and spread to Europe where it was commonly used since the 1<sup>st</sup> century AC. The general process involves dissolving gold in liquid mercury to create an amalgam, applying the amalgam to the desired surface, and heating the surface to evaporate the mercury, leaving a golden surface of typically 5 - 20  $\mu\text{m}$  thickness behind.

Fire gilding stayed the dominant form of gilding from the beginning of the Christian Era up to the middle of the 19<sup>th</sup> century. Some less widespread alternatives were *depletion gilding* and *powder gilding*. The first of these applies a form of chemical etching by oxidizing the undesired compounds out of the outermost layer of the surface. The latter is a form of color painting as it disperses the fine gold powder in a binder.

There are two significant drawbacks to fire gilding that eventually lead to its almost complete abolishment in the mid 19<sup>th</sup> century. It is more expensive than other techniques and, with evaporating mercury, a huge health hazard. As soon as electricity generators were invented, people started thinking about utilizing the electric power for electrolytic deposition of gold on metals. Today it is the dominant gilding method. Alternatives are mostly applied in art and for restoration purposes. Restoration work is the only field where fire gilding is still allowed.

## 1.2 Motivation & Aim of this Work

The focus of this work is the previously described *fire gilding*. K. Anheuser identified in his work [10] that the color change from silver/grey to golden appears at around 260°C. For the goldsmith, there is no reason to further heat the material once the desired golden-colored surface is achieved. They will, therefore, interrupt the heating process and continue with polishing the material after it has cooled.

Referencing the Au-Hg-phase diagram [11] (see figure 1), it becomes clear that this is not hot enough to fully evaporate mercury from the amalgam-system as there are still stable solid Au-Hg configurations at this temperature ( $\zeta$ -phase). This observation is in agreement with empirical studies that determine the typical Hg content of fire gilded materials in the range of 5-25%, occasionally even higher. This lead many researchers to the conclusion that 5% is the natural lower limit for mercury

in fire gilded objects [10, 12, 13]

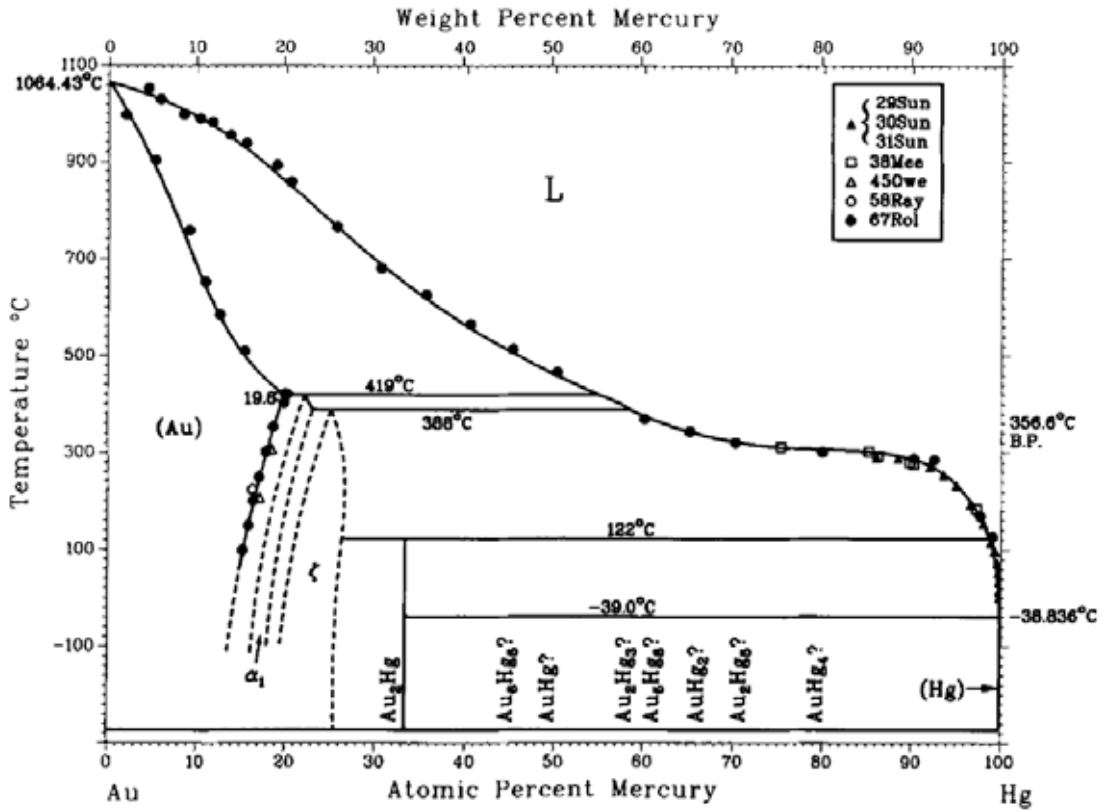


Figure 1 – Phasediagram of the Au-Hg-system under variable pressure. [11]

However, recent studies on gilded silver objects from the Antikensammlung Berlin by B. Niemeyer et al. [14] showed some unexpected results (see figure 2).

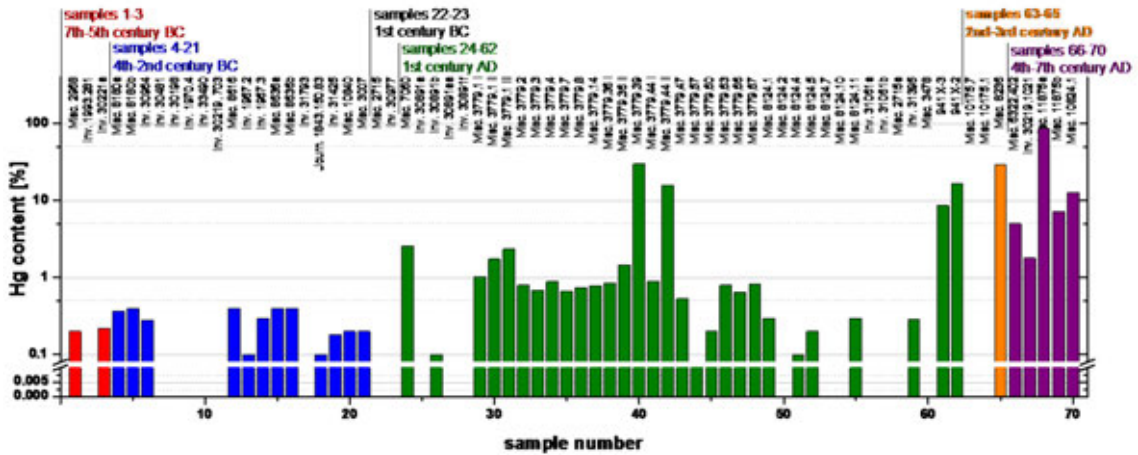


Figure 2 – Mercury contents of 70 different fire gilded silver objects from the Antikensammlung Berlin. The sample names in the upper part of the figure are the identification numbers used in the Antikensammlung. Note that the x-axis is sorted chronologically but not scaled to represent the actual age differences between the samples. [14]

The samples before the 1<sup>st</sup> century AC (shown in blue and red) show Hg contents below 0.5%, which can be explained by insufficient purification or storage of the

gold. Samples from the 2<sup>nd</sup> century onwards show elevated levels of the Hg content above the 5% threshold, which identifies them as fire gilded. Within the 1<sup>st</sup> century AC, however, there are a variety of samples with Hg contents in the region between 0.5 and 5% (e.g., samples 32-38).

These samples show that the current understanding of fire gilding might not be sufficient for a clear identification of the process and are the main motivation for this work.

This work builds on the Bachelor's thesis by this author [15] and a previous Master's thesis by S. Kuhn [16] that both investigated possibilities for a destruction free identification of fire gilding on silver and copper substrates (XRF by Kuhn and XRF combined with Neutron Activation Analysis (NAA) by Margreiter).

The Bachelor's thesis posed new questions about the Hg content within the golden layer and the behavior of mercury with time and during the gilding process. It further indicated that the Hg content is affected by the chosen substrate.

This thesis tries to answer the raised questions with a particular focus on the development of a destruction-free identification method for fire gilding in light of the recent, so far unexplained, findings of slightly elevated Hg contents. Particularly interesting is the identification of a characteristic of fire gilding beyond the sheer presence of mercury. Previous studies suggest the existence of a distinct depth profile. Which, if present, might be used for such an identification.

Additionally, this work tries to further study the suggested 5% limit as identification for fire gilding.

With these goals in mind, efforts were taken to better understand the XRF results by simulating spectra with a Monte Carlo software. Additionally, initial PIXE measurements of gilded samples were performed, aiming toward the identification of fire gilding through the combination of two or more methods with different depth resolution.

## 2 Methods

This chapter presents an overview of the methods applied during the project. It will first give a summary of the basic principles of XRF, leading into an introduction to the XMI-MSIM software package for the simulation of XRF-spectra via Monte Carlo simulations.

Concluding the XRF section of this chapter is an overview over BESSY II and the BAMline where the XRF-measurements were performed.

In the end, an overview of PIXE is given.

### 2.1 X-Ray Fluorescence Analysis

If not stated otherwise the content of this section is based on the books *X-Ray Fluorescence Spectroscopy* by R. Jenkins [17] and *Instrumentelle Analytische Chemie* by K. Cammann [18].

XRF is a qualitative and quantitative spectroscopic technique for the chemical characterization of a material. It utilizes the emission of characteristic X-rays for the identification of different chemical elements in a sample. It allows simultaneous multi-element analysis and is destruction-free.

The two basic concepts necessary for the understanding of XRF are the photoelectric effect and X-ray fluorescence.

The photoelectric effect is one of the possible interaction schemes between photons and bound atomic electrons. Other possibilities are different types of scattering, e.g., Compton-, as well as Rayleigh- and Raman-scattering, which will not be further discussed in this thesis. These phenomena are responsible for the intensity loss when radiation passes through matter, given by

$$I_A = I_0 * e^{-\mu\rho d} \quad (1)$$

with the initial intensity ( $I_0$ ), the intensity after passing the matter ( $I_A$ ), the material and wavelength dependent attenuation coefficient ( $\mu$ ), the density ( $\rho$ ), and the material thickness ( $d$ ).

If the energy ( $E$ ) of the incoming photon at the moment of collision is higher than the binding energy ( $\phi$ ) of the electron, the electron is ejected from the atom and leaves the shell as a *photoelectron* with a kinetic energy of  $E-\phi$ , leaving an ion behind. This is the *photoelectric effect* as described by A. Einstein in 1905, earning him a Nobel prize in 1921 [19]. XRF utilizes X-ray radiation to achieve this effect with high-binding-energy-electrons of inner electron shells. The remaining ions, therefore, have an electron vacancy on a low energy shell, making them excited ions.

The source of the incident/primary X-rays is discussed in section 2.1.2.

Deexcitation happens through the emission of characteristic X-rays. In this process, an energetically higher electron of the same atom fills the lower energy vacancy. The energy difference between the upper and lower electron state is emitted as a photon in the X-ray frequency region. The energy differences between the various

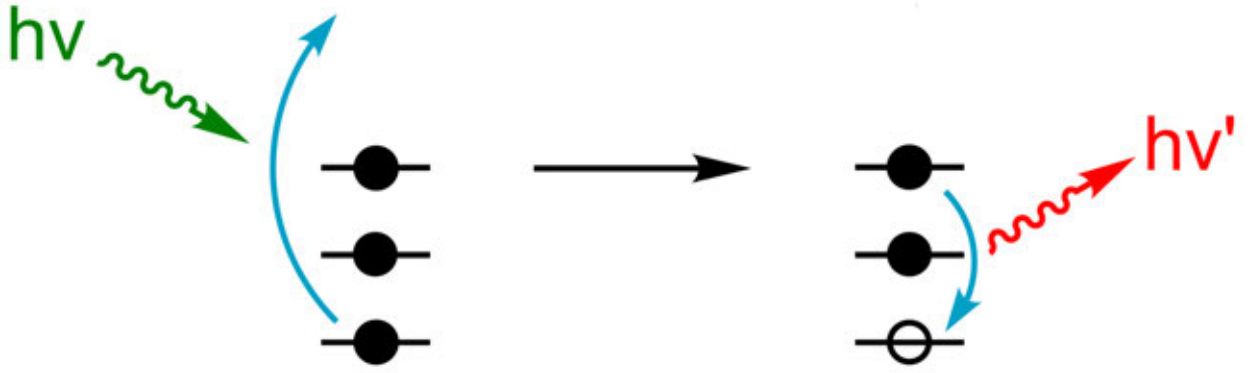


**Figure 3** – The figure shows the schematic basis of XRF. Photoelectric effect (left) and emission of characteristic X-rays afterwards (right).

energy levels are element specific and, therefore, suitable for element identification and quantification.

The process is visualized in figure 3.

BESSY II applies synchrotron radiation as a primary photon source for XRF analysis, spanning a wide area of the electromagnetic spectrum. Therefore, different electrons can be knocked out of the atom. Furthermore, there are a variety of potential electrons to fill the emerging vacancy, resulting in a large number of possible deexcitation routes and emitted characteristic X-rays.

However, upon observing the emitted wavelengths, the so-called *diagram lines*, it becomes clear that a set of selection rules apply to the deexcitation. To understand these rules, a short introduction to the electron configuration is necessary.

A consequence of the Pauli exclusion principle is that every electron in an atom is uniquely described by the four quantum numbers  $n$ ,  $l$ ,  $m$ , and  $s$ . With the principal quantum number ( $n$ ) taking positive integer values and correlating to the electron shells in Bohr's atomic model ( $K=1$ ,  $L=2$ ,  $M=3, \dots$ ). The angular quantum number ( $l$ ) with integer numbers from 0 to  $n-1$  represents the orbitals occupied by the electrons ( $l=0 \rightarrow s$ ,  $l=1 \rightarrow p$ ,  $l=2 \rightarrow d$ , ...). Leaving the magnetic quantum number ( $m$ ) with values from  $-l$  to  $+l$  and the spin quantum number ( $s$ ) with a value of either  $+\frac{1}{2}$  or  $-\frac{1}{2}$ .

Due to spin-orbit coupling, the interaction of the intrinsic angular momentum of the electron (i.e., its spin) and the orbital angular momentum, the total angular momentum ( $J$ ) is introduced as

$$J = s + l. \quad (2)$$

Combing these quantum numbers gives the *transition levels* as shown in table 1.

With this established, the selection rules for XRF are

- $\Delta n \geq 1$
- $\Delta l = \pm 1$
- $\Delta J = \pm 1$ , or 0

**Table 1** – The table shows the construction of transition levels by combining the quantum numbers  $n$ ,  $l$ , and  $J$ . Table taken from [17]

Transition Group	$n$	$l$	$J$
$K$	1	0	$\frac{1}{2}$
$L_I$	2	0	$\frac{1}{2}$
$L_{II}$	2	1	$\frac{1}{2}$
$L_{III}$	2	1	$\frac{3}{2}$
$M_I$	3	0	$\frac{1}{2}$
$M_{II}$	3	1	$\frac{1}{2}$
$M_{III}$	3	1	$\frac{3}{2}$
$M_{IV}$	3	2	$\frac{3}{2}$
$M_V$	3	2	$\frac{5}{2}$
$N_I$	4	0	$\frac{1}{2}$
$N_{II}$	4	1	$\frac{1}{2}$
$N_{III}$	4	1	$\frac{3}{2}$
$N_{IV}$	4	2	$\frac{3}{2}$
$N_V$	4	2	$\frac{5}{2}$
$N_{VI}$	4	3	$\frac{5}{2}$
$N_{VII}$	4	3	$\frac{7}{2}$

There exists a variety of ways to denote a spectroscopic transition [20]. The widespread *Siegbahn notation* is based upon relative intensities of lines. Notations take the form  $K\alpha_1$ . The capital letter denotes the shell of the initially produced vacancy and the following greek letter a set of transition lines grouped by their relative intensities, with  $\alpha$  being the set with highest intensities,  $\beta$  the set with slightly lower intensities, and so on. An index Arabic numeral is used to further distinguish between lines in the corresponding set. In some cases, a Latin numeral is given as a superscript to the greek letter if it is discovered that a line consists of a doublet.

The problem with this nomenclature is its unsystematic nature. From this, a variety of difficulties arise, starting with the small amount of information transferred with this system. That is why another notation system was introduced in the 90s, called the *IUPAC notation*.

It follows a simple structure, two transition/X-ray levels separated by a hyphen (e.g.,  $L_3 - K$ ). The small difference between the previously shown notation for transition levels (see tab. 1) is that the X-ray levels are prescribed with an Arabic numeral subscript in the IUPAC notation, as opposed to the previously used Latin subscript. The first level denotes the vacancy and the second level the X-ray level of the electron filling the vacancy. The correspondence between the Siegbahn and the IUPAC notation for the nomenclature of XRF-lines is shown in table 2.

Some additional effects might cause confusion when studying XRF-spectra, mainly the Auger effect, and dual ionization. The Auger effect describes the possibility of the characteristic energy being radiationless transmitted to an electron with the energy  $E_{X-ray} - E_{Binding}$ . This effect reduces the number of characteristic X-rays from a certain energy level and is usually taken into account by the so-called *fluorescent yield*.

On the other hand, dual ionization can lead to the emergence of low-intensity *satellite lines* in the XRF-spectrum. Dual ionization hereby means an additional

**Table 2** – Correspondence between Siegbahn and IUPAC Notations for the nomenclature of XRF-lines. Table taken from [17]

Siegbahn	IUPAC	Siegbahn	IUPAC	Siegbahn	IUPAC
$K\alpha_1$	$K-L_3$	$L\alpha_1$	$L_3-M_5$	$L\gamma_1$	$L_2-N_4$
$K\alpha_2$	$K-L_2$	$L\alpha_2$	$L_3-M_4$	$L\gamma_2$	$L_1-N_2$
$K\beta_1$	$K-M_3$	$L\beta_1$	$L_2-M_4$	$L\gamma_3$	$L_1-N_3$
$K\beta_2^I$	$K-N_3$	$L\beta_2$	$L_3-M_5$	$L\gamma_4$	$L_1-O_3$
$K\beta_2^{II}$	$K-N_2$	$L\beta_3$	$L_3-N_5$	$L\gamma_4'$	$L_1-O_2$
$K\beta_3$	$K-M_2$	$L\beta_4$	$L_1-M_3$	$L\gamma_5$	$L_2-N_1$
$K\beta_4^I$	$K-N_5$	$L\beta_5$	$L_1-M_2$	$L\gamma_6$	$L_2-O_4$
$K\beta_4^{II}$	$K-N_4$	$L\beta_6$	$L_3-O_{4,5}$	$L\gamma_8$	$L_2-O_1$
$K\beta_{4x}$	$K-N_4$	$L\beta_7$	$L_3-N_1$	$L\gamma_8'$	$L_2-N_{6,7}$
$K\beta_5^I$	$K-M_5$	$L\beta_7$	$L_3-N_{6,7}$	$L\eta$	$L_2-M_1$
$K\beta_5^{II}$	$K-M_4$	$L\beta_9$	$L_1-M_5$	$L\epsilon$	$L_3-M_1$
		$L\beta_{10}$	$L_1-M_4$	$L_\zeta$	$L_3-M_2$
		$L\beta_{15}$	$L_3-N_4$	$L_\tau$	$L_3-M_3$
		$L\beta_{17}$	$L_2-M_3$	$L_u$	$L_3-N_{6,7}$
				$L_v$	$L_2-N_{6,7}$

ionization of an atom during the lifetime of the excited state.

### 2.1.1 XMI-MSIM

As part of this work, energy dispersive XRF-spectra were simulated using the XMI-MSIM software by T. Schoonjans. This section will give a short introduction to the software [21].

The samples simulated with XMI-MSIM consist of parallel homogeneous layers of the desired composition. The X-ray source, as well as the geometry of the set-up, are fully adjustable.

The Monte Carlo code simulates the path of individual photons in the material, starting from a given direction and energy. Each photon path consists of a number of subsequent interactions that potentially change the direction and energy of the photon. Between every interaction, the photon travels a step length ( $S_i$ ) interaction-free. In the end, the photon is either completely absorbed or leaves the material again, where it can potentially be detected. Figure 4 demonstrates the basic step of such an interaction.

The basis for the simulation is a generated probability for, among others, step length, interaction mode, and property adjustment based on the starting configuration, as well as a random number generation system applied to the probabilities to determine the taken path. More details are given in [21].

### 2.1.2 BESSY II

The electron storage ring BESSY II is a third-generation synchrotron radiation source operated by the **H**elmholtz-**Z**entrum **B**erlin für **M**aterialien und **E**nergie (HZB) (see figure 5). It employs a two-part set-up with a full energy injection system and the actual storage ring. The injection system consists of a 70-kV DC thermionic gun, a racetrack microtron for the initial acceleration of the electron,

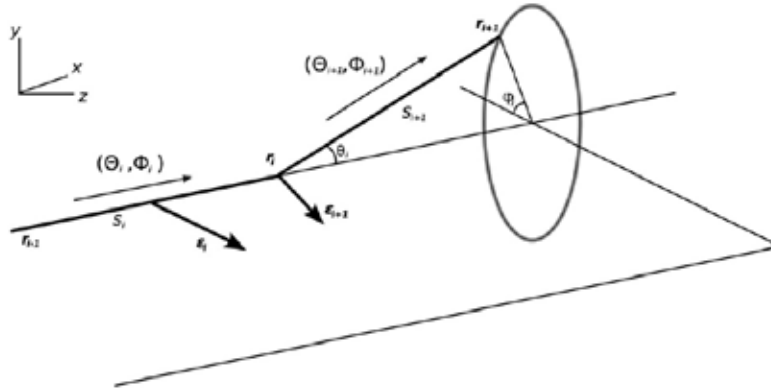


**Figure 4** – Basic picture of a photon-matter interaction as simulated by the Monte Carlo code. Shown here is the change of photon properties  $(\Theta_i, \Phi_i, \epsilon_i)$  as a result of a photon-matter interaction,  $r_i$ , with the step length,  $S_i$  between interactions. Picture taken from [22].

and a 1.7 GeV booster synchrotron. [23]

The 1.7 GeV electrons are injected in the storage ring, where they are kept on a circular path of 240 m circumference by 32 deflector magnets.

Synchrotron radiation is radiation emitted by accelerated charges. It was first observed by Elder et al. in 1947 [25] and covers a broad part of the electromagnetic spectrum, ranging from infrared light to hard X-rays. In BESSY II, the photons used for our experiments are generated in undulators, periodically arranged sets of dipole magnets, forcing the electrons to oscillate and emitting radiation as a consequence (see 6).

#### 2.1.2.1 BAMline [27, 28]

The BAMline is a hard X-ray beamline set up and operated by the **BundesAnstalt für Materialforschung und -prüfung** (BAM), the Federal German institute for material research and testing and the **Physikalisch-Technische Bundesanstalt** (PTB), the German national institute for metrology.

A superconducting 7T wavelength shifter is the source for the photons utilized on the beamline. Afterward, two individual monochromators (a **Double Multilayer Monochromator** (DMM) and a **Double Crystal Monochromator** (DCM)) are the main optical elements that can be used individually or in combination. The beamline set-up is shown schematically in figure 7.

Choosing the monochromator is mainly a consideration of resolution vs. flux. The DMM selects a relatively wide energy band but allows for a high flux rate, while the DCM does the opposite, sacrificing flux rate for a small energy band. The DCM uses diffraction as described by Bragg's law for monochromatization, while the DMM utilizes interference from photons reflected of different layers for the monochromatization.

Not shown in figure 7 are a set of **Compound Refractive Lenses** (CRLs), which are used in the set-up to focus the monochromatized high-intensity beam to a diameter of  $\sim 1\mu\text{m}$  [30]. They are shown, together with the Si(Li) semiconductor detector, in

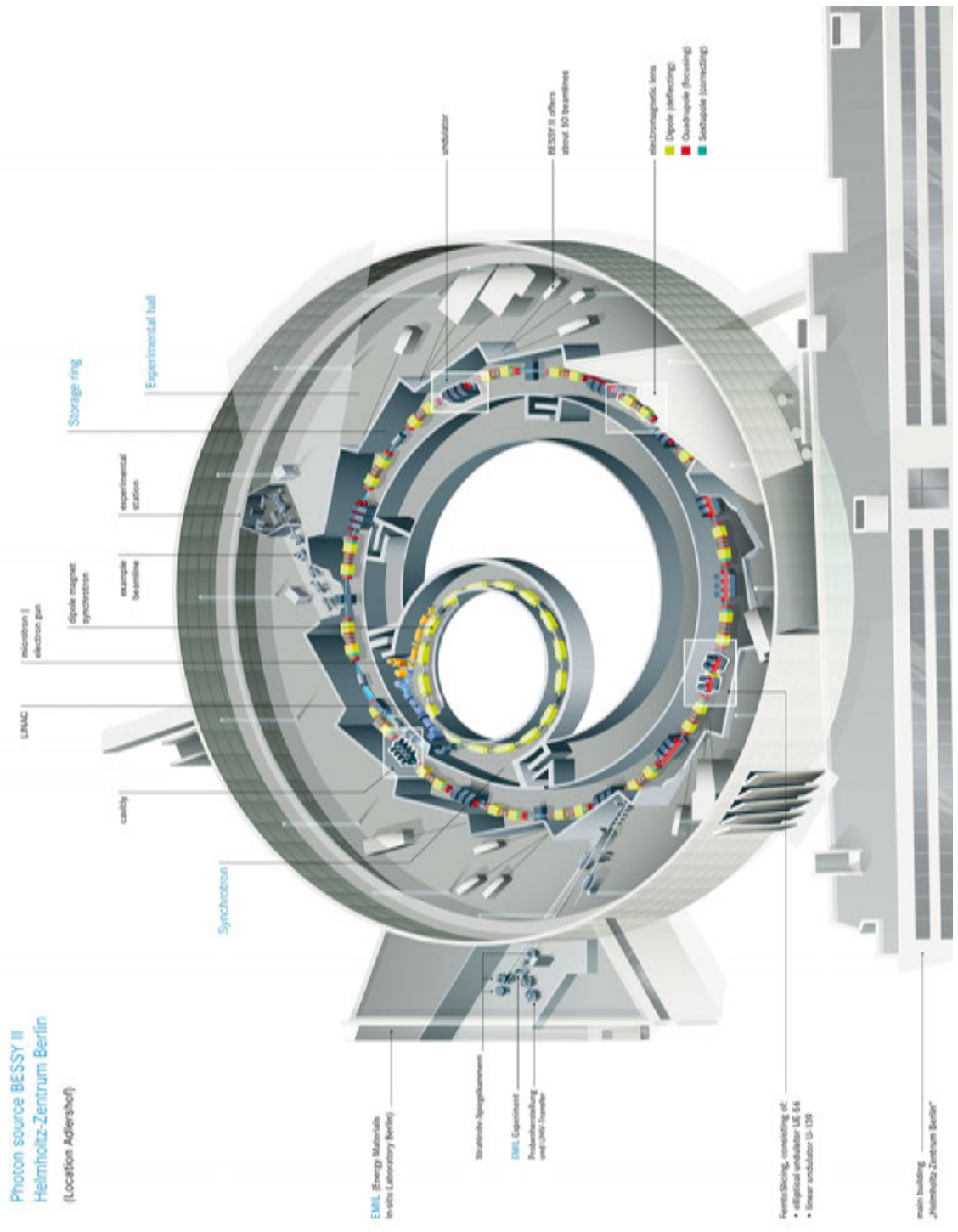
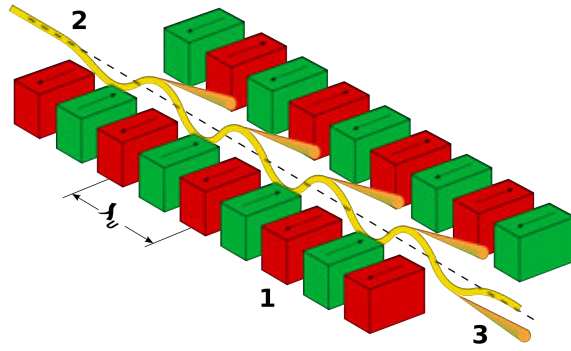
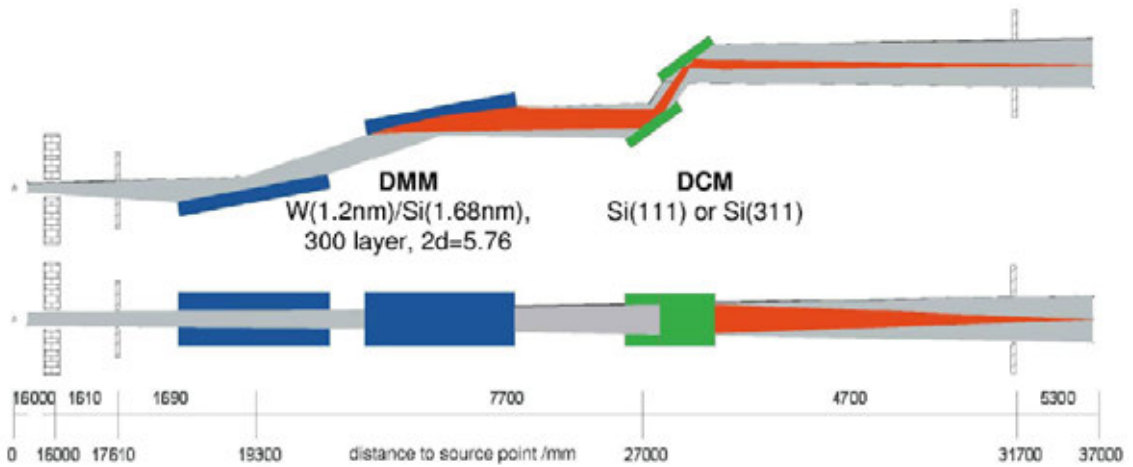


Figure 5 – Components of BESSY II. [24].



**Figure 6** – Schematic picture of an undulator. The figure shows the alternating arrangement of dipole magnets (1) with the spatial period ( $\lambda_u$ ), the electron beam (2), and the synchrotron radiation (3). [26].



**Figure 7** – Beam path at the BAMline (top: side view, bottom: top view). Originating from a 7T wavelength shifter, the beam can be monochromatized with a DMM and/or a DCM. [29].

figure 8. A schematic picture of the set-up is shown in figure 9  
 Through this set-up, the samples were irradiated with X-rays with a 40 keV excitation energy.

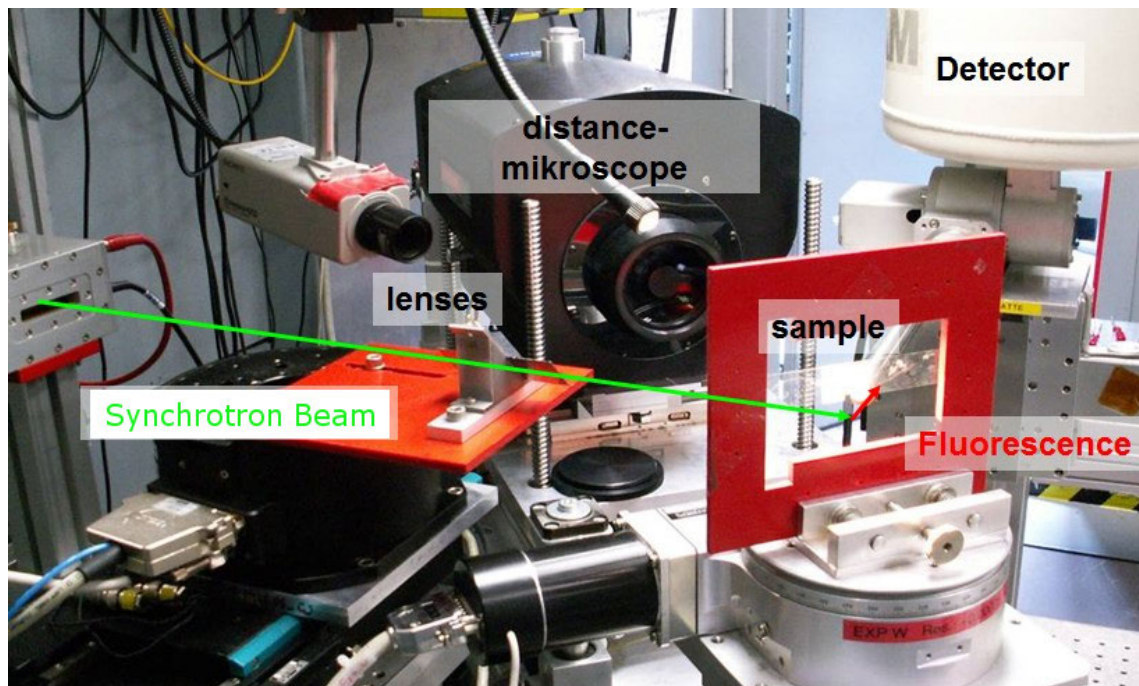


**Figure 8** – Picture of the measurement set up at the BAMline. The synchrotron beam (green) passes through the CRLs, focussing the beam to  $\sim 1\mu\text{m}$  in diameter. After hitting the sample at a  $45^\circ$  angle, fixed into a motorized holder, the characteristic X-rays are emitted as fluorescence. They are detected in the Si(Li) semiconductor detector. Also in the picture are a camera and a microscope to aim the beam at a particular spot of the sample.

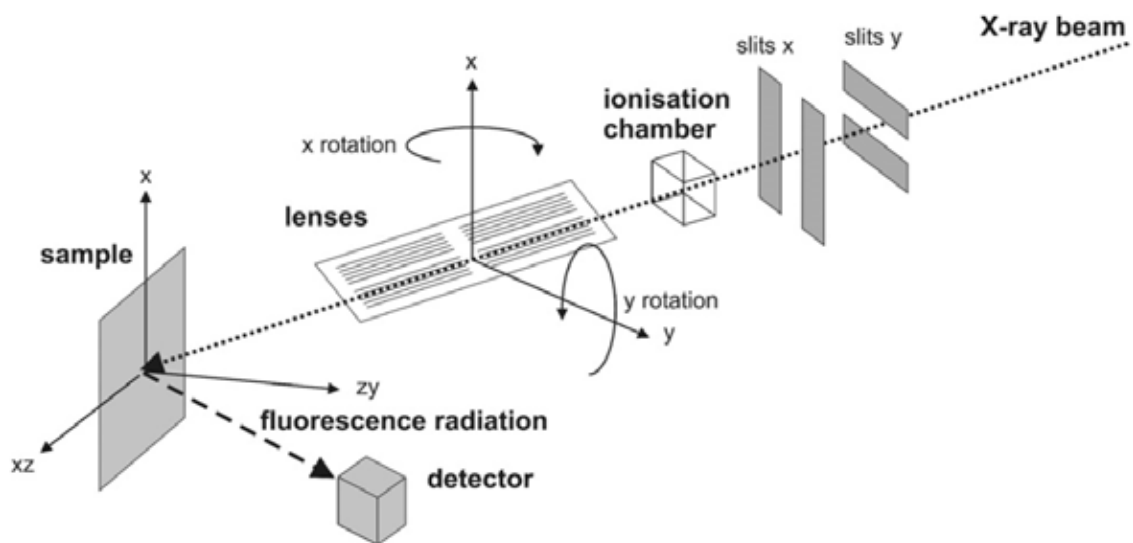


**Figure 9** – Schematic picture of the measurement set up at the BAMline with CRLs.

## 2.2 Particle-Induced X-ray Emission [31]

Just like XRF, PIXE is an analytical method based on the emission of characteristic X-rays after inner-shell ionization. The conceptual difference is the utilization of accelerated ions, instead of primary X-rays for the ionization.

It is a destruction free method for qualitative and quantitative analysis of liquid and solid samples.

## 3 Experimental

This chapter deals with the experiments performed for the thesis at hand. Starting with an introduction into the process of fire gilding as performed in the lab, continuing with an overview of the measurements, and ending with a detailed look into the gathered results.

### 3.1 Sample Preparation

The preparation of the samples for this thesis was performed in the lab by the author.

The amalgam paste was created by mixing leaves of pure 24 kt gold (*Wasner Blattgold >99%*) with mercury five times the mass of the gold. When the materials came into contact, the gold immediately started to dissolve in mercury and greyed out while the amalgam was formed. The mix was thoroughly kneaded until the amalgam paste had a uniform color; the desired texture of the amalgam is thick and firm but ductile. If the texture is too firm more mercury can be added to reach the desired ductility.

However, adding more mercury should be avoided if possible, as it may lead to a very thin and visibly uneven golden layer on the substrate.

Before the paste can be applied to the substrate, the silver and copper sheets had to be cleaned with water and acetone. This is sufficient for the silver sheets. The copper sheets additionally had to be treated with diluted acetic acid to remove the oxide layer.

Previously, the copper sheets were treated with a mercury salt to amalgamate the surface of the substrate [15] as it is modern practice during the gilding process [32]. This greatly simplifies the application of the gold amalgam on the copper substrate but is not a historical approach to the method. The step was, therefore, substituted for most of the samples with the diluted acetic acid cleansing, which can be assumed to be a more historically accurate approach.

The amalgam paste was then applied to the prepared substrates with a spatula and brush. The paste sticks very well to the silver sheet and can be easily spread with the brush. One has to be careful when applying the amalgam to the silver. Due to the ease of application, the resulting amalgam layer can become very thin and result in only a faint golden color at the end.

The opposite is true for the copper. Even with the pretreatment, the amalgam does not stick very well to the surface, and the application has to be done with care. The best method was to press small pieces of the paste onto the substrate with a spatula and then very carefully using the brush to smoothen out the surface.

After that, the covered sheet was heated in the open flame of a bunsen burner at the top of the colorless flame, with the covered side facing upwards. This is important since the color is the indicator for when the heating can be stopped. Figure 10 demonstrates the three stages of the heating process. Shortly after the color-change to gold, the substrate should be taken out of the flame and left to cool. If done correctly, the surface looks like shown in figure 11.

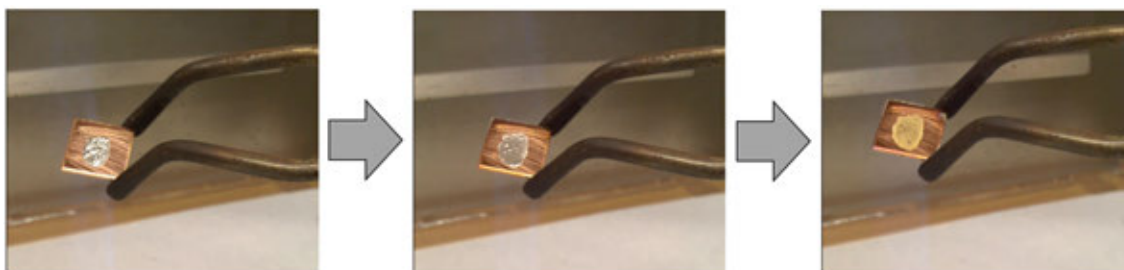


**Figure 10** – Picture series of the heating process during fire gilding of a copper substrate. Left: Glossy amalgam with a lot of excess liquid mercury bubbling off at the start of heating. Middle: Dull silver/grey amalgam after around 15 seconds of heating. Right: Desired golden surface after an abrupt color change at the end of the heating process (around 20 seconds of heating).

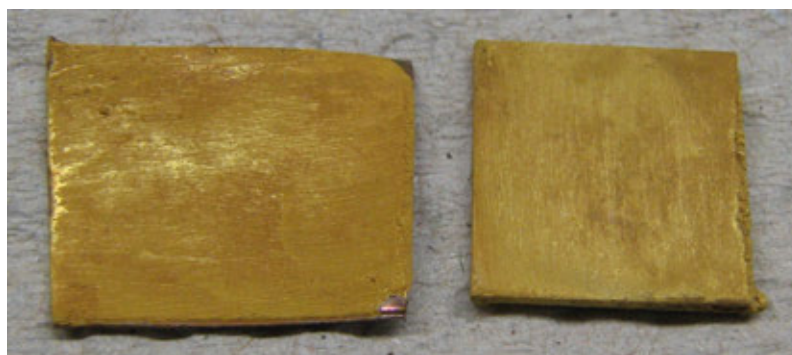


**Figure 11** – Unpolished fire gilded metal sheets. Copper substrate on the left, silver substrate on the right. [15].

The results of two common mistakes during the gilding process are shown in figure 12. The picture on the right shows the typical results of fire gilding on copper when the amalgam was not applied with enough care, or the treatment with acetic acid was insufficient. The picture on the left shows the results of heating the samples too long. On silver, the golden layer fades out, mostly due to diffusion between the amalgam and the substrate, and on copper, the heat finally leads to oxidization of the substrate. The layer blackens and crumbles off.

After cooling, the dull golden layers can be hardpolished to get the expected glossy golden surface.

The described method was assessed during the already quoted Bachelor's thesis by this author. For that work, the lab-prepared samples were compared to samples made by a professional goldsmith, specialized in fire gilding. While the professional samples look more uniform with the naked eye, the results showed that the lab samples compared well for homogeneity of the Hg content across one sample and between different samples. This demonstrated that research on the gilded layers can be performed on lab-made samples and does not require preparation by a professional goldsmith.

Another step performed for the thesis was the application of a second golden layer, done similar to the first. It was shown that this did not affect the Hg content in a meaningful manner. The step was, therefore, omitted for the work at hand.



**Figure 12** – Pictures of fire gilding done wrong, showcasing some common difficulties and mistakes. Left: Heating for too long. The golden color fades out on the silver substrate due to diffusion, and the golden layer crumbling off the copper substrate due to oxidation. Right: Irregular golden layer on copper substrates due to insufficiently adherent amalgam before heating. [15].

### 3.1.1 Additional or adjusted steps

During the course of this work, this standard method was sometimes adjusted or extended to prepare samples for different measurements.

An adjustment was made to prepare samples for the measurement of a temperature profile. For this purpose, long copper substrates (3-4 cm long) were covered in the amalgam and then heated only on the very tip. This creates a heat gradient along the sample. Heating was stopped when the side in the open flame took the desired golden color.

To analyze the effects of aging, some samples were heated for a fixed time span at defined temperatures in an oven.

Cross section samples were embedded in *Struers EpoFix* epoxy-resin after the gilding process. They were cut and polished in the HZB workshop.

## 3.2 Measurements

This section will give a detailed overview of the performed measurements. It is structured after the final purpose of the measurements, i.e., spectra simulation, preparation analysis, artificial aging, cross section analysis, and one-off PIXE measurements.

### 3.2.1 Spectra simulation

Utilizing the Monte Carlo simulation software XMI-MSIM, 54 different XRF spectra of a homogeneous amalgam layer with 9 different Hg contents and 6 different layer thicknesses (see table 3) were simulated. Details on the simulation parameters are given in the appendix.

**Table 3** – An overview over the different simulation parameters used with the XMI-MSIM Monte Carlo software. The amalgam layer was treated as a single homogenous layer of varying composition and thickness.

<b>Hg content (Hg/(Au+Hg))</b>	0.1	0.15	0.2	0.25	0.3	0.35	0.4	0.45	0.5
<b>Layer Thickness [<math>\mu\text{m}</math>]</b>	0.1	1	3	10	20	100			

This was done to evaluate the influence of self-absorption and scattering effects and at least rudimentary correcting for it, if necessary.

### 3.2.2 Preparation analysis

The purpose of the measurements in this category was to answer questions directly relating to how the preparation method influences the final results. This is done to, on the one hand, better understand the process itself and, on the other hand, determine the necessary preparation steps to acquire consistent and robust results, and eliminating redundant steps. Two different kinds of measurements were performed for this.

**Influence of polish.** The first is the evaluation of whether polish might affect the quantification of the Hg content. Half of a prepared sample was polished with agate stone. The other half was left untouched (an example is given in fig 13).

Three silver and three copper samples were prepared with this method. The copper sheets had previously been used in the Bachelor's thesis and are therefore treated with mercury salt for amalgamation during the gilding process.

The copper sheets were measured six times each on the polished and unpolished sides. The silver sheets were scanned from the polished to the unpolished side with 16 equidistant measuring points.

**Temperature profile** As described above, a total of three temperature profile samples on copper substrates were prepared. A first temperature profile sample was



**Figure 13** – Fire gilded silver (left) and copper (right) sheets. The left side of each sample is polished.

**Table 4** – Table of samples analysed for the influence of polish on the determined Hg content.

Substrate	Name	Description	Measurements
Ag	SE1	single layer gilding, prepared in the lab	line scan with 16 data points from polished to unpolished
	SE2	single layer gilding, prepared in the lab	line scan with 16 data points from polished to unpolished
	SD1	double layer gilding, prepared in the lab	line scan with 16 data points from polished to unpolished
Cu	C3	double layer gilding, prepared by a goldsmith	six times each on polished and unpolished side
	C5	double layer gilding, prepared by a goldsmith	six times each on polished and unpolished side
	CE1	single layer gilding, prepared in the lab	six times each on polished and unpolished side

made to understand the gilding process from the perspective of the Au-Hg phase diagram 1 (sample: cg). It is important to note that this sample was still prepared with amalgamation as pretreatment.

With this in mind, two additional temperature profile samples were analyzed during a later beamtime. These samples were prepared to explicitly compare the influence of amalgamation on the Hg content during the gilding process. This is why one of the samples (tg-Hg) was prepared with previous amalgamation and the other one (tg) without.

A picture of the very first temperature profile sample is shown in figure 14.



**Figure 14** – Picture of a temperature gradient sample (cg). The sample was heated from the left side.

Measurement details are given in table 5.

**Table 5** – Table of samples prepared for temperature gradient analysis during the gilding process. Sample cg was thoroughly analyzed, samples tp and tp-Hg were prepared to verify previous results.

sample	description	measurements	stepsize [ $\mu\text{m}$ ]
cg	amalgamized copper substrate	10 line scans with 482 data points each	100
tp	non-amalgamized copper substrate	1 line scan with 162 data points	100
tp-Hg	amalgamized copper substrate	1 line scan with 138 data points	100

### 3.2.3 Artificial aging

Historic fire gilding samples can be as old as 2000 years. For this reason, a series of samples and measurements were dedicated to the understanding of how fire gilded layers evolve over time.

It was assumed that by rule-of-thumb, the reaction rate of a given process (here: the aging) doubles with a temperature increase of 10 °C. Through this, aging was artificially accelerated by heating the samples for a set amount of time at a set temperature.

To be able to perform all measurements during one beamtime, the effect of aging was not tested with a single sample (heated, measured, heated, measured, ...), but with a set of samples heated for different amounts of time.

An example of such a set of samples is shown in fig 15.



**Figure 15** – Exemplary picture of a series of artificial aging samples. Artificial aging time increases from left to right. Copper substrates at the top, silver substrates at the bottom. The samples were treated with 200°C between 0.25 (left) and 21 (right) days, more details can be found in table 8 for samples Cu/Ag I-x.

A total of 60 samples were analyzed for this aspect of the ratio, split into three different series of measurements.

The first sample set was prepared for an earlier beamtime and meant as a preliminary test run to build on for later sample sets. An overview of the preparation- and measuring parameters is given in table 6.

Based on these preliminary results, the next set of samples was prepared. The samples are purely copper substrates. This time, three sample sets were heat-treated at three different temperatures for clearly defined periods of time to allow for a comparison between the sets. The amalgam mixtures used for the preparation of the different sample sets were prepared at different times, leaving room for potential differences in the gilding based on the amalgam mixture. An overview of the preparation- and measuring parameters of the 18 samples is given in table 7.

The last set of samples consists of a total of 30 samples, 15 each on copper and silver. To give the best possible basis for comparison, the same amalgam mixture was used for the preparation of samples on the same substrate. An overview of the preparation- and measuring parameters of the 18 samples is given in table 8.

**Table 6** – Table of preparation- and measuringparameter of the artificial aging samples for preliminary measurements. The measurement series was used to establish a foundation to plan further artificial aging measurement series.

Sample	Substrate	Comment	Time [d]	Temperature [°C]	Measuring-time [s]	Measuring-points
Ag0	Silver	-	-	-	10	9
Ag1	Silver	-	1	250	10	9
Ag2	Silver	-	3	130	10	9
Ag3	Silver	-	3	160	10	9
Ag4	Silver	-	3	200	10	9
Ag5	Silver	-	10	150	10	9
Ag6	Silver	-	24	150	10	9
Cu0	Copper	amalgamized	-	-	10	9
Cu1	Copper	amalgamized	1	250	10	9
Cu2	Copper	amalgamized	3	130	10	9
Cu3	Copper	amalgamized	3	160	10	9
Cu4	Copper	amalgamized	3	200	10	9
Cu5	Copper	amalgamized	10	150	10	9
Cu6	Copper	amalgamized	24	150	10	9

**Table 7** – Table of preparation- and measuringparameters of copper substrate artificial aging samples for a systematic measurement series of the effect of aging a sample at different temperatures and for different periods of time. The t20, t19, and t18 samples were prepared from different amalgam mixtures.

Sample	Temperature [°C]	Time [d]	Measuring-time [s]	Measuring-points
t20	200	0	10	9
		0.25	10	27
		1	10	27
		3	10	27
		7	10	27
		10	10	27
t19	190	0	10	27
		0.25	10	27
		1	10	27
		3	10	27
		7	10	27
		10	10	27
t18	180	0	10	27
		0.25	10	27
		1	10	27
		3	10	27
		7	10	27
		10	10	27

### 3.2.4 Cross section analysis

The previously established aim of this work was the establishment of a destruction free method for the unambiguous identification of fire gilding apart from the sheer presence of mercury in the sample.

For this, it is necessary to identify specific characteristics in fire gilded samples, e.g., a distinct depth profile, and subsequently establishing a method to detect this specific characteristic. The results of previous projects lead to the assumption that mercury distribution in the fire gilded layer is not homogenous but varies across the cross section of a gilded layer. This is in partial agreement with K. Anheuser, who found an enrichment of mercury at the interface of fire gilded silver substrates if

**Table 8** – Table of preparation- and measuringparameters of artificial aging samples for a systematic measurement series of the effect of aging a sample at different temperatures and for different periods of time. Measurements were performed with copper and silver substrates. All samples were prepared from the same amalgam mixture.

Sample		Temperature [°C]	Time [d]	Measuring-points	Measuring-time [s]	
Ag/Cu	I	200	I	0.25	3	10
			II	1	2	10
			III	4	3	10
			IV	7	3	10
			V	21	3	10
	II	180	I	0.25	3	10
			II	1	3	10
			III	4	3	10
			IV	7	3	10
			V	21	3	10
	III	160	I	0.25	3	10
			II	1	3	10
			III	4	3	10
			IV	7	3	10
			V	21	3	10

these were pretreated with a mercury salt [10].

If such an interface could be found, a destruction free method for its identification could be developed, e.g., combination of different techniques with different information depths.

Therefore, cross section analysis was a significant part of this project. The general idea for this kind of research was to physically cut a fire gilded sample and analyze the cross section with precise, small step XRF measurements, as they are possible at the BAMline at BESSY II.

To achieve this, samples were embedded in an epoxy-resin and subsequently cut and polished. Figure 16 shows an exemplary picture of samples prepared as described.

A total of 16 samples were prepared this way. 11 on silver substrates, 5 on copper substrates.

During the first beamtime for this sample set, two mapping scans on one fire gilded Cu substrate and one fire gilded Ag substrate were performed. These measurements were initial proof-of-concept tests. The details are given in table 9.

**Table 9** – Measurement parameters for two cross section analysis samples (1 Cu substrate, 1 Ag substrate). Both measurements are mapping scans consisting of a variety of linescans across the sample cross section. The samples were embedded and cut at an angle to increase the cross section surface.

Sample	Substrate	Stepsize [ $\mu\text{m}$ ]	Measuringpoints	Comment
pra	Cu	1	426 (71 in 6 lines)	goldsmith, amalgamized
prb	Ag	0.1	2005 (401 in 5 lines)	



**Figure 16** – Exemplary picture of fire gilded copper and silver substrates embedded in epoxyresin and subsequently cut and polished for cross section analysis. Top: Silver substrate; Bottom: Copper substrate

Based on previous results, the measurements during the next beamtime focused solely on cross section analysis of fire gilded Ag substrates. The primary goal was to verify previous observations. Details are given in table 10.

**Table 10** – Measurement parameters for 6 Ag substrate cross section analysis samples. Samples pr1 - pr6 were measured with 3 individual linescans each, sample pr8 was analyzed with a mapping scan.

Sample	Stepsize [μm]	Measuring-time [s]	Measuring-points	Comment	
pr1	1	2	10	48	
	2	2	10	49	
	3	2	10	55	
pr2	1	2	10	41	
	2	2	10	47	
	3	2	10	42	
pr3	1	2	10	50	double gilded
	2	2	10	34	double gilded
	3	2	10	34	double gilded
pr4	1	2	10	34	
	2	2	10	47	
	3	2	10	62	
pr6	1	2	10	40	
	2	2	10	44	
	3	2	10	43	
pr8	1	1	10	6204 (44 in 141 lines)	Mapping

The last set of measurements regarding cross section analysis focussed once again on Ag and Cu substrates, but with different purposes. Ag substrates were prepared by varying the time between the application of the amalgam and the Hg evaporation,

ranging from immediate heating to a resting period of a whole week. Cu samples were measured with the main goal of verifying the previous observations.

**Table 11** – Measurement parameters for 8 cross section analysis samples (4 Ag substrates, 4 Cu substrates). One Ag and one Cu substrate sample were analyzed with a mapping scan, the other samples with 4 individual linescans each. The Ag sample nomenclature (s0x) denotes the number of days x between the application of the amalgam and the heating process.

Ag				Cu				
Sample	Measuring-time [s]	Stepsize [ $\mu\text{m}$ ]	Measuring-points	Sample	Measuring-time [s]	Stepsize [ $\mu\text{m}$ ]	Measuring-points	
s00	900	20	2470 (130 in 19 lines)	c01	100	20	2340 (117 in 20 lines)	
s01	500	15	2	67	500	15	2	26
	600	15	2	67	600	15	2	26
	700	10	2	67	700	15	2	26
	800	15	2	67	800	15	2	26
s03	500	10	2	67	500	15	2	73
	600	10	2	62	600	15	2	76
	700	15	2	67	700	15	2	75
	800	10	2	67	800	15	2	70
s07	500	15	2	67	500	15	2	71
	600	15	2	67	600	15	2	71
	700	15	2	70	700	15	2	79
	800	15	2	67	800	15	2	70

### 3.2.5 PIXE

To perform a first test on whether profiling information might be extracted, a set of samples (Ag 0 to Ag I-V), previously used for artificial aging analysis, was measured with PIXE at the Liese-Meitner-Campus of the HZB. The samples are shown in figure 17 and the measurement parameters in table 12.



**Figure 17** – Fire gilded silver substrates on a PIXE sample holder. The samples were previously used during the artificial aging analysis. Information about the samples can be found in table 8.

**Table 12** – Measurement parameters for the PIXE analysis of artificially aged fire gilded silver substrates. The samples were previously analyzed with XRF (See table 8).

Sample	Measurement-time [s]	Intensity (brutto)
0	600	71451
I I	600	71181
I II	600	70873
I III	600	70705
I IV	600	70451
I V	600	69858

### 3.3 Results

This section will give a detailed overview of the data collected during the measurements, presented in a constructive manner corresponding to the respective question. This section will not present the results of every single measurement. It instead focusses on a meaningful, sometimes exemplary presentation of the results. A more comprehensive overview of the data is given in the appendix.

Throughout this thesis, the term *Hg content* is used as the percentage of mercury within the gilding layer (consisting of Au and Hg). In praxis this usually refers to the line intensity ratio of the  $L_\alpha$  lines in the XRF spectra given by equation 3, corrected for the different self-absorption of the Hg and Au lines, as presented in the following section.

$$Hg\ content = \frac{I(Hg)}{I(Hg) + I(Au)} \quad (3)$$

The line intensities for all XRF measurements are determined by automatic fitting of the X-ray line intensities with the AXIL code [33].

#### 3.3.1 Spectra Simulation

For the evaluation of the simulation data, the  $L_{\alpha,1}$  and  $L_{\alpha,2}$  lines of Hg and Au were used.

Plotting the simulated Hg content vs. the thickness of the simulated layer yields results as shown in figure 18.

The simulation was set up in such a manner that the actual Hg content of the homogeneous mix layer was exactly 25%. However, none of the simulated Hg contents are below 26.2% and as high as 27.4%. The determined Hg content additionally significantly increases between layer thicknesses of 0.1 to 20  $\mu\text{m}$ .

This observation suggests that the  $L_\alpha$  lines of Au are more affected by self-absorption than the  $L_\alpha$  lines of Hg. The almost constant Hg content determined from samples with layer thicknesses above 30  $\mu\text{m}$  also suggests that the effective detectable penetration depth of X-rays is around 30  $\mu\text{m}$ . Which is in good agreement with the literature [34].

To adjust for this, the differences between the actual Hg content and the measured Hg content were calculated for different layer thicknesses and plotted against the measured Hg content (see figure 19). Fitting the data sets yielded equations, that can be utilized to determine the difference between the measured and the actual Hg content for a given layer thickness (see table 13).

All further results presented in this thesis were corrected for the determined difference for a layer of 20  $\mu\text{m}$  thickness, the typical thickness observed in our samples.

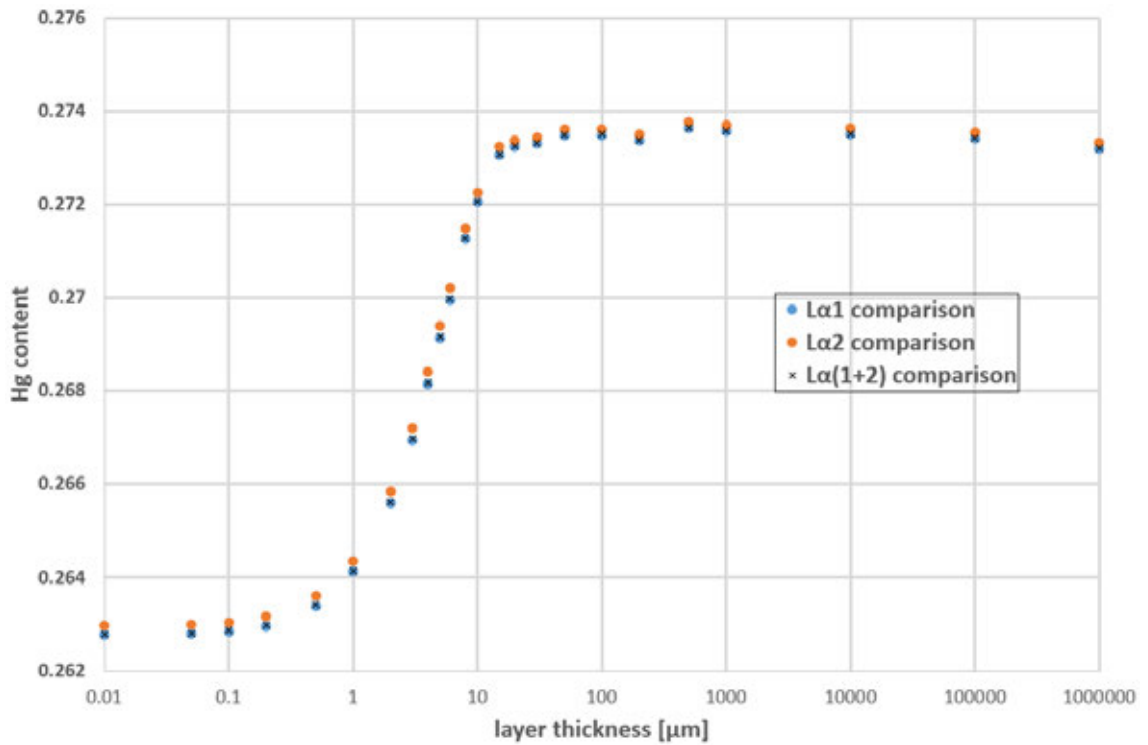


**Figure 18** – Hg content determined from simulated XRF spectra of a homogenous layer with varying thickness and a fixed Hg content of 25%. The figure shows Hg contents determined from the  $L_{\alpha,1}$  line, the  $L_{\alpha,2}$  line, and the sum of both lines.

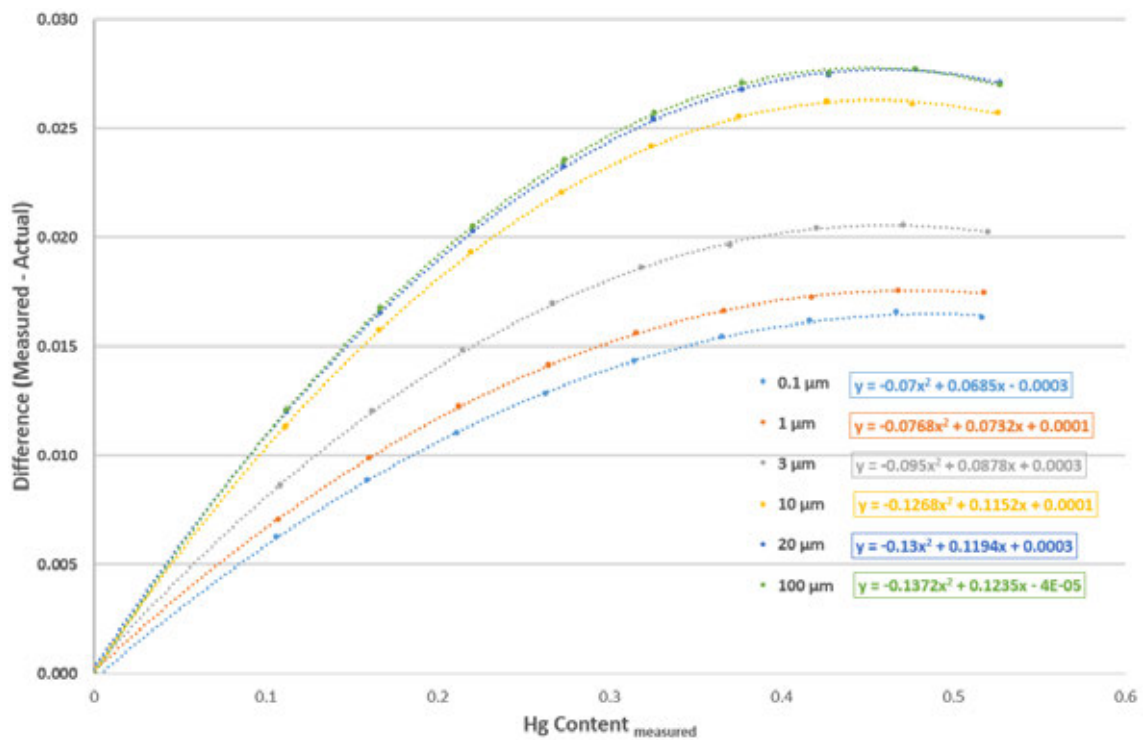


**Figure 19** – Difference between the measured and the actual Hg content plotted against the measured Hg content for various layer thicknesses. A fit through the data sets yields an equation to determine the difference between measured and actual Hg content for a given layer thickness.

**Table 13** – The table lists the equations that, for a set layer thickness, can be used to determine the difference between measured and actual Hg content.  $x$  refers to the measured Hg content.

Layer Thickness [ $\mu\text{m}$ ]	Hg content difference (Measured - Actual) [x: Measured Hg content]
0.1	$y = -0.07x^2 + 0.0685x - 0.0003$
1	$y = -0.0768x^2 + 0.0732x + 0.0001$
3	$y = -0.095x^2 + 0.0878x + 0.0003$
10	$y = -0.1268x^2 + 0.1152x + 0.0001$
20	$y = -0.13x^2 + 0.1194x + 0.0003$
100	$y = -0.1372x^2 + 0.1235x - 4\text{E-}05$

### 3.3.2 Polishing & Temperature Profile

**Polish** Figure 20 shows the results regarding the evaluation of the influence of polish on the measured Hg content.

The linescans on the silver samples result in trendlines with varying slopes from slightly positive to slightly negative. Additionally, the polish edge is not apparent from the data. This suggests that polish does not affect the measured Hg content of fire gilded silver samples. The small slopes are probably due to inhomogeneities of the gilding layer.

A similar conclusion can be drawn from the copper substrate data. Samples C5 and CE3 show no difference between the polished and unpolished side. An exception is sample C3, which shows a significant difference between the measurements on the polished vs. measurements on the unpolished side. Here it appears as if polishing decreases the determined Hg content. In the light of the other samples, however, this difference most likely also arises from inhomogeneities.

**Temperature profile** Figure 21 shows the development of the Hg content during heating. The sample used for this measurement was prepared with the additional amalgamation step before the gold amalgam was applied. To verify that the general structure of this temperature profile is the same regardless of amalgamation, a single linescan over two other (one with amalgamation, the other one without) temperature profile samples were performed. A figure comparing the measurements is shown in the appendix.

After a steady decrease of the Hg content for about 20 mm, the Hg content drops over the course of less than 1 mm, remaining almost constant afterwards with a small decrease during the last 15 mm. This behavior can be understood if it is viewed through the lens of the phase diagram (see figure 22).

The rapid decrease in Hg content corresponds to the phase transition from the grey  $\text{Au}_2\text{Hg}$  phase to the golden  $\text{Au}_3\text{Hg}$  phase with excess liquid mercury. Due to the high temperature, the excess mercury evaporates almost immediately, causing the sudden drop in Hg content.

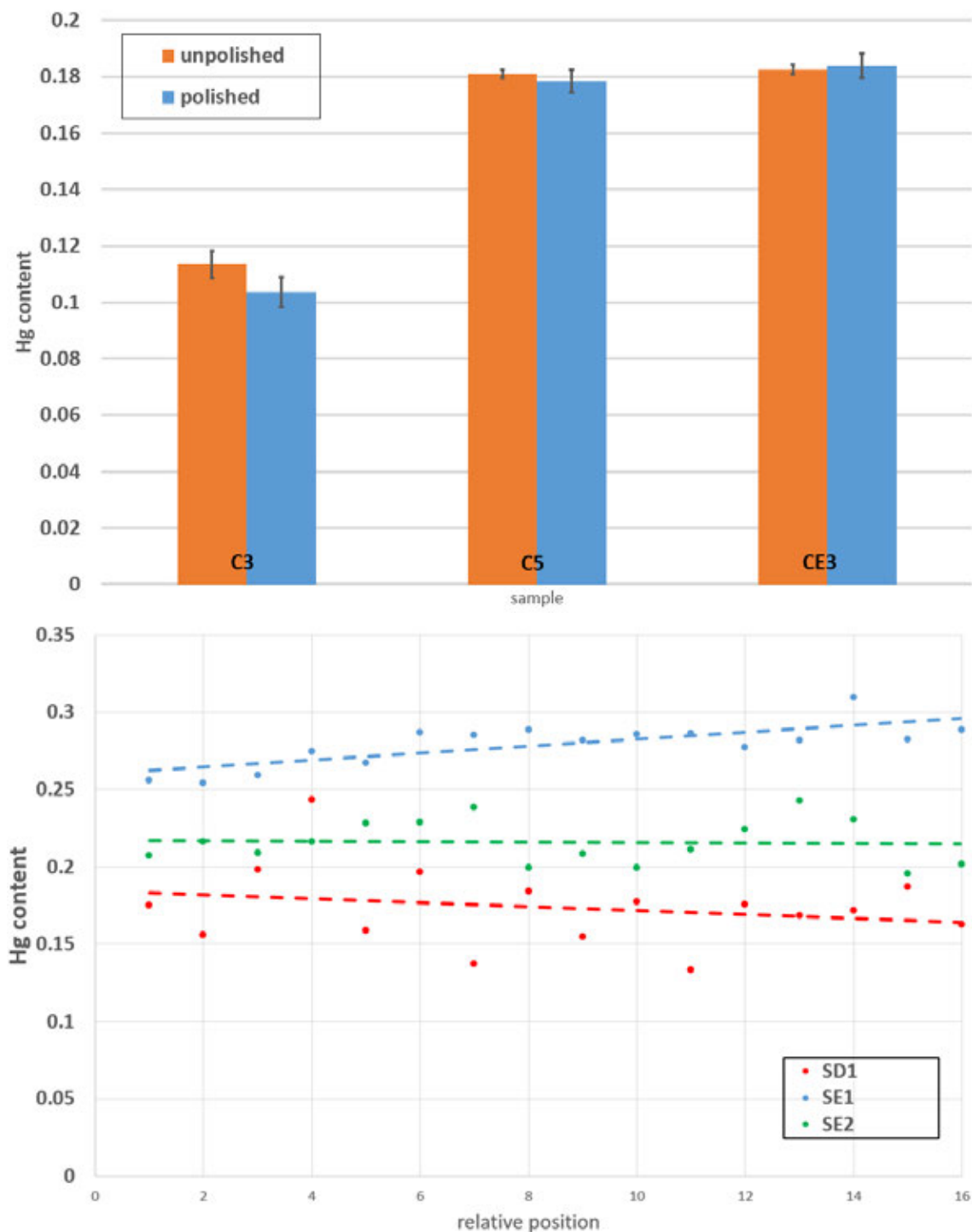


**Figure 20** – Analysis of the influence of polish on the measured Hg content in a sample on copper and silver. Top: Three fire gilded copper substrates measured on the polished and unpolished side, shown are the mean values of 9 measurements on each side. Bottom: Three fire gilded silver substrates measured as a linescan from the polished to the unpolished side. Also added is a trendline as a rough visualization of the general trend.

### 3.3.3 Artificial Aging

Three different measurement series for artificial aging were performed. The first was meant as a test run for later measurements to choose a good temperature for the analysis, that would, on the one hand, simulate long aging in a small amount of

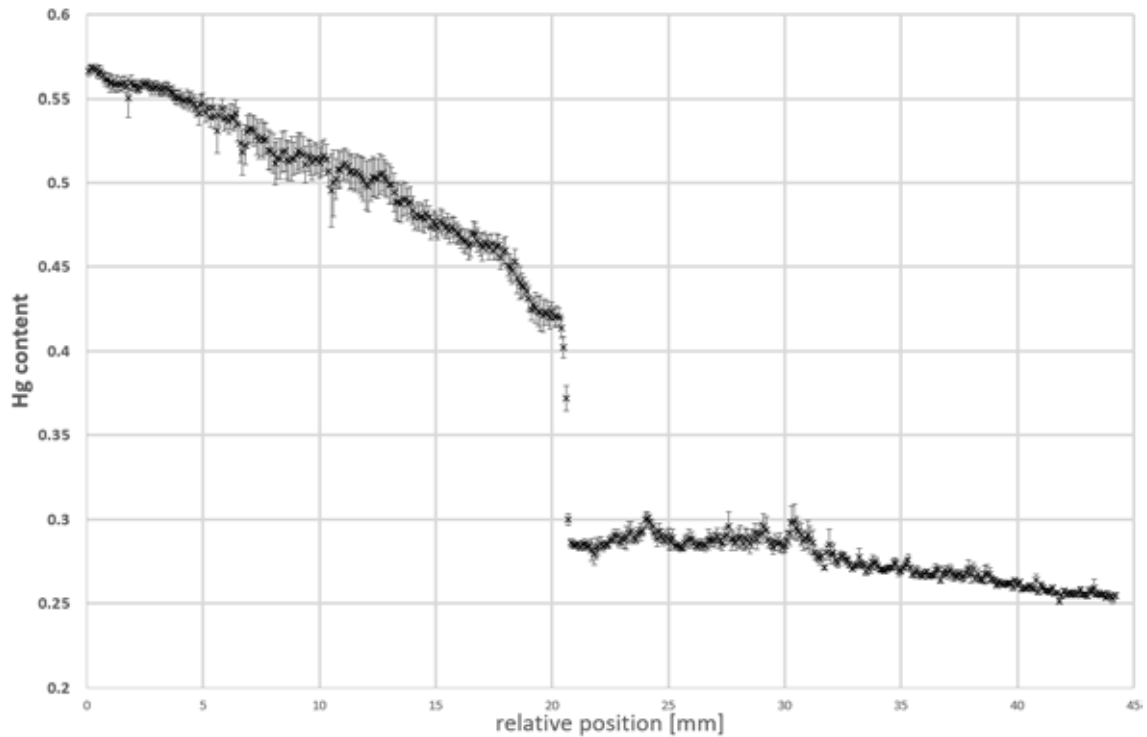


**Figure 21** – Development of the Hg content during fire gilding on a copper substrate. The sample was measured from the unheated side (left) to the heated side (right) in 10 linescans. The data points were adjusted so that the leap in the middle of the figure fell on the same relative position for all linescans. Displayed are the mean values of these adjusted linescans with their standard deviation.

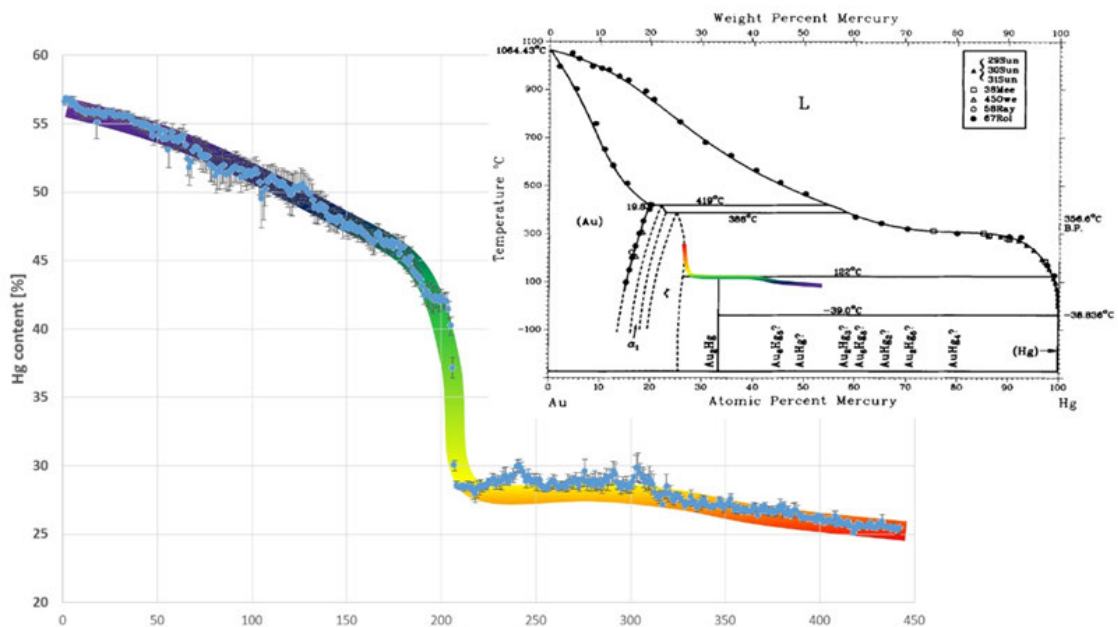


**Figure 22** – Development of the Hg content during fire gilding on a copper substrate in the context of the Au-Hg-phase diagram. Temperature profile on the lower left side, Phase diagram in the upper right. The color gradient is used to represent the measured data in the phase diagram, color coding different areas of the temperature profile.

time, while still leaving the sample intact, i.e., not visually destroying it. 200 °C was chosen as the maximum temperature applicable to artificial aging based on the

results.

However, the results were analyzed in light of the simulated aging time as shown in table 14 and figure 23.

**Table 14** – Table showing the rough timeperiode simulated with the artificial aging at a fixed temperature for a set amount of time, if the +10 °C → 2x reaction rate rule-of-thumb applies.

Sample	Heating Time [d]	Temperature [°C]	Simulated Aging [a]
Cu/Ag	0	RT	0.1
	1	250	22966.8
	2	130	16.8
	3	160	134.6
	4	200	2153.1
	5	150	224.3
	6	150	538.3

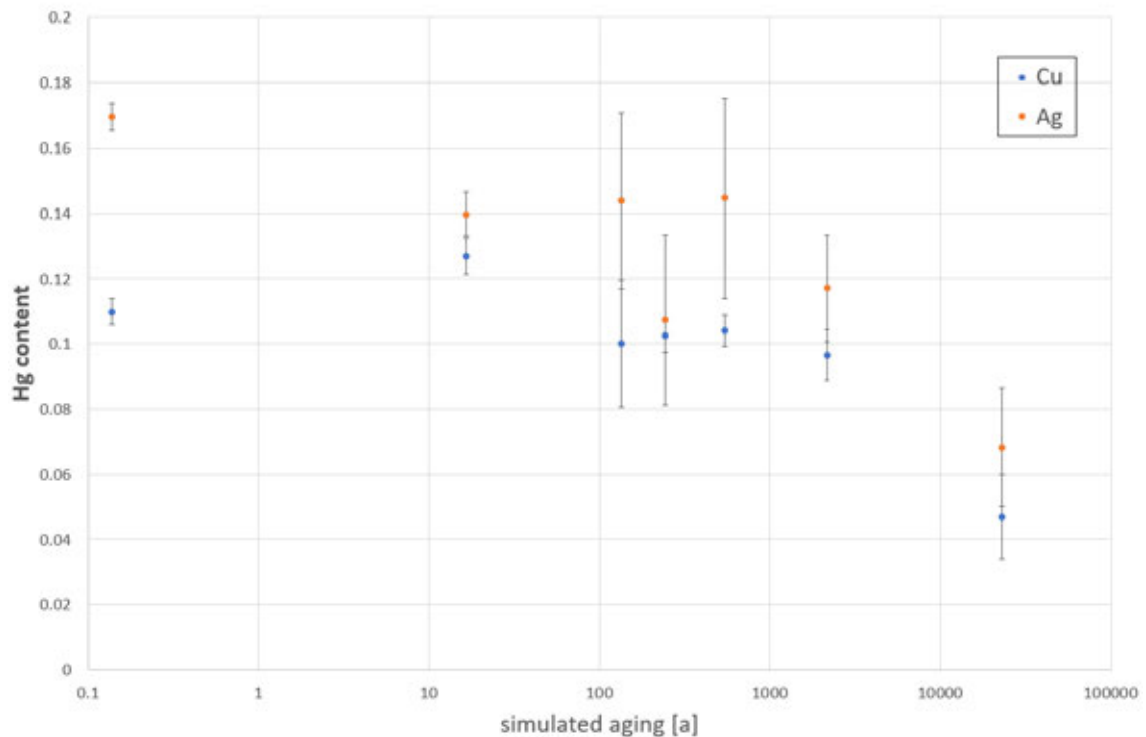


**Figure 23** – The determined Hg content in artificially aged fire gilded Ag and Cu substrates plotted against the simulated years as shown in table 14.

Based on these results, it seems like the reduction of the Hg content due to aging is minimal even over a few millennia. The measurement series was, however, not optimized for such an analysis. Interesting to note here, is that even samples Ag01 and Cu01 do not undercut the 5 % Hg content, although the samples are visually destroyed. The last observation is particularly interesting for the initial question of the validity of the 5% minimum as accepted in the literature.

The follow-up measurement series investigated the influence of varying heating times at different temperatures. The results are presented in figure 24.

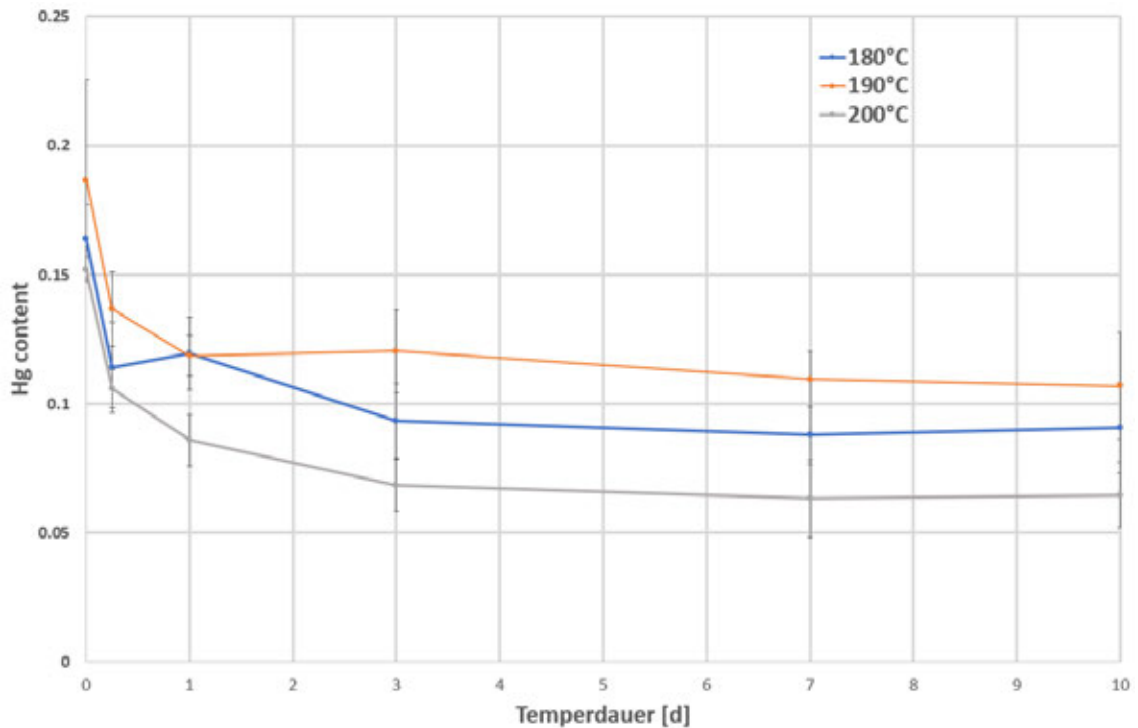


**Figure 24** – Absolute Hg contents of the artificially aged fire gilded Cu substrates plotted against the heating time, for different temperatures.

For a better comparison between the different temperatures, the Hg contents were converted from their absolute values to relative values, compared to the highest Hg content in the respective aging series. These relative values were plotted against the simulated time, calculated, just like before, from the rule-of-thumb that a temperature increase of 10 °C doubles the reaction time. This plot is shown in figure 25.

The results suggest a logarithmic relation between the Hg content and the simulated aging period.

The follow-up measurement series, yielded inconclusive results, mainly due to the small number of measurement points on the samples. A figure showing these results can be found in the appendix.

As a closing remark for the artificial aging results, single measurements yielded Hg contents as low as 3.4 % and 4.5 % for averaged measurements on the AgI-V sample. They undercut the accepted 5 % limit, although a more thorough examination of the sample might be necessary, as demonstrated by the inconclusive results of the whole set of measurements.

### 3.3.4 Cross section Analysis

Figure 26 presents the key findings regarding the cross section analysis of this thesis.

Cross section analysis shows a distinct distribution of the Hg content across the sample for Ag substrates. Figure 26 shows an Hg accumulation at the interface

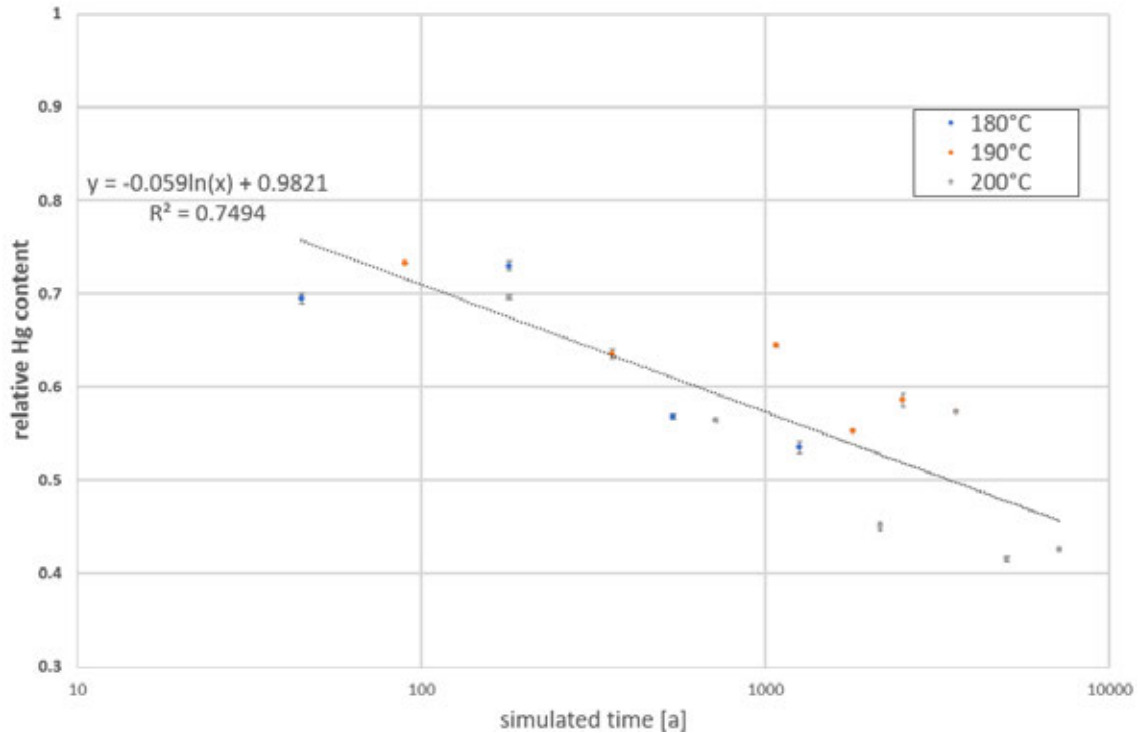


**Figure 25** – Plotting relative Hg contents of artificially aged Cu substrates at different temperatures against the simulated aging periode. Simulated aging periode determined with the assumption that  $+10\text{ }^{\circ}\text{C} \rightarrow 2x$  reaction rate. The data suggest a weak logarithmic relation between both parameters.

between gilded layer and Ag substrate. This cannot be observed for Cu substrates.

Another observation not as apparent as the Hg accumulation, is that the determined Hg content after the interface, i.e., within the substrate, stays constant for more than  $10\text{ }\mu\text{m}$  in Ag substrates and starts fluctuating just a few  $\mu\text{m}$  in the substrate for Cu. Both observations, likely depend on amalgam/Hg diffusion into the substrate. They suggest that diffusion is significantly easier into an Ag substrate than a Cu substrate. This is in agreement with previous studies [10].

A general observation is that the development of Hg-accumulated interfaces does not depend on amalgamation previous to the application of the Au-amalgam. None of our Ag substrates were treated with the Hg-salt, but all showed the Hg accumulation, while none of the Cu substrates, independent of previous amalgamation, show such an accumulation. In fact, the Cu sample in figure 26 was treated with Hg-salt. This is a new insight into the process and a direct contradiction to previous findings by K. Anheuser.

The formation of the Hg-accumulated interface is ascribed to the diffusion behavior of Hg/amalgam. This leads to the question if the peculiarity of the accumulation is affected by the time between the application of the Au-amalgam and the Hg evaporation. A set of measurements was dedicated to this question.

The Hg profile was recorded in a small mapping scan across the four samples. To allow a comparison, the absolute Hg contents were converted to relative values and the maxima of the profile placed atop of each other. This is shown in figure 28.

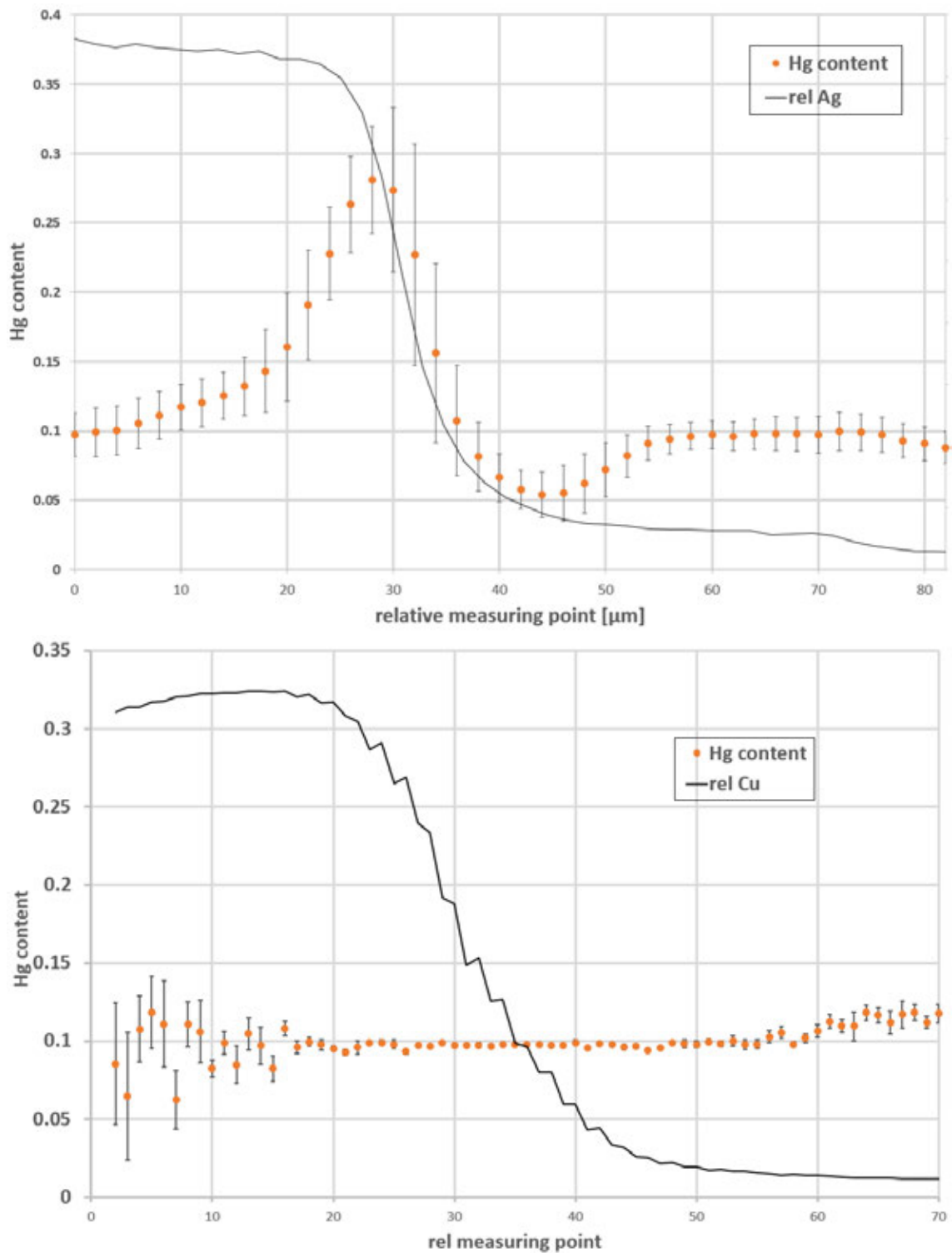


**Figure 26** – cross section analysis of a fire gilded silver (top) and copper (bottom) substrate. The figure shows the development of the Hg content across the interface of the substrate and the gilding. The surface of the sample is on the right side of the diagram.

The diagrams were the results of mapping scans across the interfaces of the samples (Ag: pr8 from June 2017; Cu: pra from February 2017). Apart from the Hg content, the diagrams also display a line for the relative intensities of the substrate. They are shown to visualize the position of the interface and were used to line-up the different linescans of the mapping to produce this picture, also giving the uncertainties as the standard deviation.

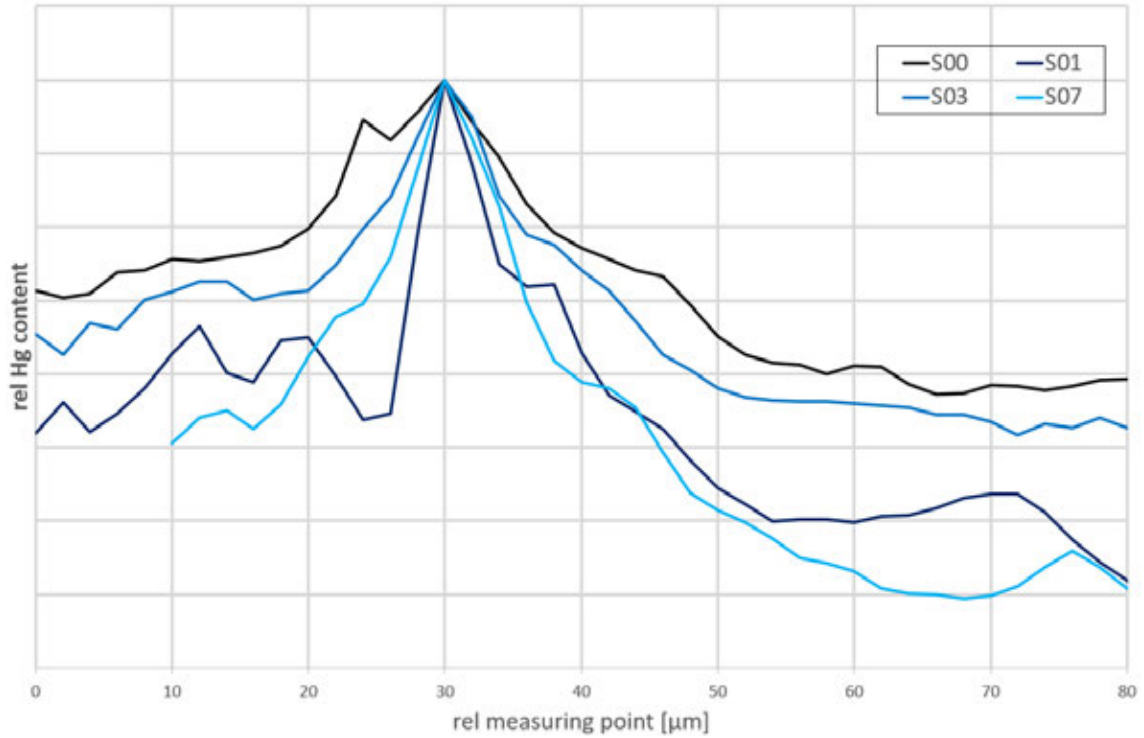


**Figure 27** – Comparison of relative Hg content distribution across the interface of fire gilded Ag substrates with different amounts of time between Au-amalgam application and Hg evaporation. The sample label should be read as S0x, with x representing the number of days between application and evaporation. Uncertainties omitted for readability.

Due to relatively high uncertainties, the reliability of figure 28 is limited. However, it appears that the accumulation of Hg at the interface does, in fact, depend on the time between application and evaporation, since the accumulation is least distinct for the sample heated immediately after the amalgam application (S00).

A conclusive statement about the time period over which the accumulation takes place, be it minutes, hours, or days, is not possible from our results. The initial accumulation, however, only seems to take a few minutes, since it is already clearly visible in S00.

### 3.3.5 PIXE

Figure 28 shows the Hg contents of the artificial aging samples AgI-I to AgI-V as determined with XRF and PIXE.

The measurement shows significantly higher Hg contents in the samples when determined with PIXE vs. XRF. There is no trivial explanation for this observation, based on our previous results. The only trivial explanation would be that PIXE reaches the accumulated Hg at the interface with a higher information depth, but this cannot be the case. The L lines, used for the determination of the Hg content in both methods, allow for a maximum information depth of 20-30  $\mu\text{m}$ , as evidenced by our simulations. This depth is reached by the more energetic primary X-rays used in the XRF.

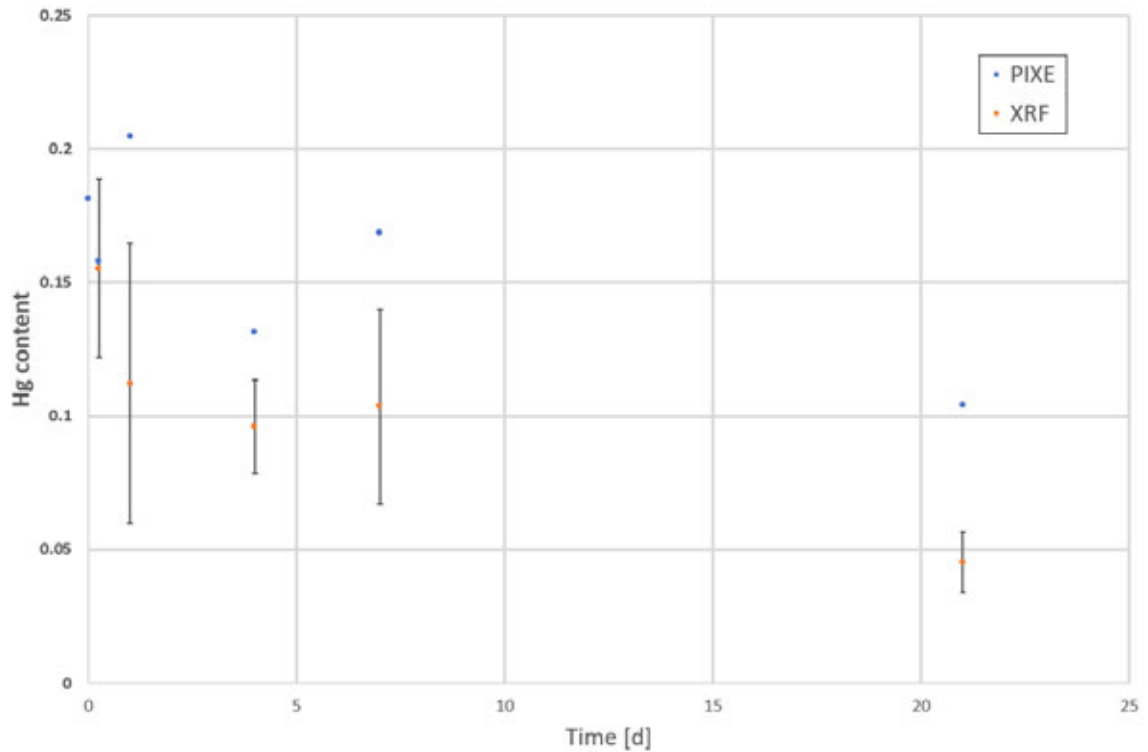


**Figure 28** – Hg contents of fire gilded and artificially aged Ag substrates as determined with XRF and PIXE.

## 4 Conclusion

This work is an important step towards the establishment of a new, destruction-free method for the identification of fire gilding.

The main achievements are a better understanding of the Hg behavior during gilding, the development of a correction term to adjust the XRF measured Hg content to better represent the actual sample composition, insight into the development of measured Hg content during aging processes, the identification of a characteristic Hg-accumulation at the interface of fire gilded Ag substrates, and the confirmation of the accepted 5% minimum.

### 4.1 Summary

Through Monte Carlo simulations of XRF spectra, we were able to find a correction term to adjust the measured Hg contents to match the actual batch composition of the sample.

We also found the information depth of XRF applied to fire gilded layers to be between 20-30  $\mu\text{m}$ , a value in accordance with the literature.

Regarding sample preparation, the measurements showed that polish does not significantly affect the measured Hg content.

The creation of a temperature profile sample enabled us to study the Hg content during the Hg evaporation. With this, the gilding process could be integrated into the Au-Hg phase diagram.

Preliminary results from the analysis of artificial aging, suggest a logarithmic relation between the Hg content and the passed aging period. We also found some individual measurements that clearly undercut the assumed lower Hg content limit of 5%. However, these single measurements might not represent the whole sample.

Careful examination of cross sections of fire gilded Ag and Cu substrates found an Hg accumulation at the interface of Ag substrates, not present in Cu substrates and independent from amalgamation of the substrate before the application of the Au-amalgam. An observation directly contradicting previously held assumptions. Further tests suggest that the formation of this Hg accumulation might depend on the time between the application of the Au-amalgam and the Hg-evaporation.

First PIXE measurements showed Hg contents higher than those determined with XRF. An observation yet to be understood.

## 4.2 Discussion

The initial observation leading into this work was that fire gilded silver objects from the 1<sup>st</sup> century AD in the Antikensammlung Berlin showed low but clearly enriched Hg contents between 0.5% and 5%. The previously accepted minimum limit for Hg in fire gilded objects was 5%, leaving the Hg contents in those 1<sup>st</sup> century samples unexplained. This led to two main questions that this work tried to answer.

1. Does the 5% minimum need to be abolished? → Can we reliably reproduce such low Hg contents in our own fire gilded samples, and if so, how?
2. Can we find another method for the identification of fire gilding except for the pure presence of mercury, based on other characteristics of fire gilded samples?

In all our samples, a Hg content of even 10 % is rarely undercut, there are very few single measurements that undercut the accepted 5% minimum limit, but those were part of an inconclusive measurement series and not robust enough to challenge the accepted limit. Additionally, even visually destroyed artificial aging samples showed Hg contents above the limit. Generally speaking, our measurements further substantiate the accepted limit.

In addition, we found a Hg enrichment at the interface of fire gilded Ag substrates that forms quickly after the amalgam application due to diffusion of Ag and Hg. There is no reason to believe that this characteristic vanishes over time. Furthermore with the Hg enrichment at the interface, superficial influences of the sample surrounding such as leaching in the soil will not significantly reduce the measured Hg content.

From all this, the elevated Hg content in the 1<sup>st</sup> century samples of the Antikensammlung Berlin are probably not explained by fire gilding. The concentration of these samples on a single century, on the other hand, suggests that they are probably not explained with flawed XRF measurements.

It might be, that our artificial aging measurements were not sufficient as they did not take the influences of the environment, e.g. soil, into account, potentially leading to a depletion of Hg in the sample.

On the other hand, the Hg contents might be explained by the introduction of Hg into the workspace of ancient goldsmiths during the 1<sup>st</sup> century. Hg vapor could diffuse into separately stored gold, which would be used for other types of gilding.

Regarding identification beyond the 5% criteria, we found a clear Hg enrichment at the interface of fire gilded Ag substrates. This characteristic could be identified with destruction-free methods by combining techniques with different depth information. Some preliminary tests were performed during this thesis, such as PIXE measurements with yet to be understood results and a rough series of low angle measurements with inconclusive results, probably due to suboptimal surface conditions.

No characteristic of fire gilded Cu substrates could be found.

### 4.3 Outlook

Although some important steps toward a new destruction-free identification approach, at least for Ag substrates, were made, no such method could yet be established. Low-angle scans do not seem to be practical due to the surface condition of the samples. Neutron activation analysis as a bulk method was tested in a previous work with insufficient results. The application of this method to historical samples is also quite difficult.

PIXE seems like a promising method, especially in combination with XRF. However, this work showed that a variety of parameters might affect the detection of the interface, e.g. varying thickness or even parameters during the preparation of the samples. This leaves such analysis far outside the scope of this thesis.

Further investigation into the development of the interface through cross section analysis of artificially aged samples and temperature profile samples are suggested.

## References

- [1] W. A. Oddy. “Gilding through the ages”. *Gold Bulletin* 14.2 (1981), pp. 75–79.
- [2] W. A. Oddy. “Gilding: an outline of the technological history of the plating of gold on to silver or copper in the Old World”. *Endeavour* 15.1 (1991). A Modern Approach to the Protection of the Environment, pp. 29–33. ISSN: 0160-9327.
- [3] P. A. Lins and W. A. Oddy. “The origins of mercury gilding”. *Journal of Archaeological Science* 2.4 (1975), pp. 365–373.
- [4] E. Darque-Ceretti and M. Aucouturier. “Gilding for matter decoration and sublimation. A brief history of the artisanal technical know-how”. *1st International Conference on Innovation in ArtResearch and Technology*, 2013.
- [5] A. V. Anikin. *Gold*. Verlag Die Wirtschaft, 1987.
- [6] M. E. L. Mallowan. “Excavations at Brak and Chagar Bazar”. *Iraq* 9.1947 (1947), p. 1.
- [7] Pliny the Elder. *Naturalis Historia*. Venice :Thomas de Blavis, de Alexandria, p. 626.
- [8] O. Vittori. “Pliny the Elder on gilding”. *Endeavour* 3.3 (1979), pp. 128–131.
- [9] H. Rackham and E. H. Warmington. *Pliny: Natural History, Bd. 33-35*. Mass. and London: Loeb, 1952.
- [10] K. Anheuser. “Im Feuer vergoldet: Geschichte und Technik der Feuervergoldung und der Amalgamversilberung” (1999).
- [11] H. Okamoto and T. B. Massalski. “The Au-Hg (gold-mercury) system”. *Journal of Phase Equilibria* 10.1 (1989), pp. 50–58.
- [12] M. Becker, S. Bauer, and H. Meller. *Das Fürstengrab von Gommern*. Landesamt für Denkmalpflege und Archäologie Sachsen-Anhalt, Landesmuseum für . . . , 2010.
- [13] J. Wolters. “Vergolden”. *Reallexikon der Germanischen Altertumskunde* 32 (2006), pp. 179–199.
- [14] B. Niemeyer et al. “1.500 Jahre Vergoldungen auf Gefäßen und Schmuck. Eine analytische Reihenuntersuchung am Silberbestand der Berliner Antikensammlung”. Jan. 2018, p. 75. ISBN: 978-3-7749-4184-7.
- [15] R. Margreiter. “Analyse von Feuervergoldung mit Neutronenaktivierungsanalyse und Synchrotron-Röntgenfluoreszenzanalyse”. Bachelor’s Thesis. Universität zu Köln, 2016.
- [16] S. Kuhn. “Identifikation antiker Feuervergoldungen mit zerstörungsfreien Messverfahren”. Master’s Thesis. Humboldt-Universität Berlin, 2007.
- [17] R. Jenkins. *Chemical Analysis*. Vol. 152: *X-Ray Fluorescence Spectrometry*. 2nd. Wiley, 1999. ISBN: 9781118520864.
- [18] K. Cammann. “Instrumentelle Analytische Chemie”. *Spektrum-Verlag Heidelberg* (2001).
- [19] A. Einstein. “Concerning an heuristic point of view toward the emission and transformation of light”. *American Journal of Physics* 33.5 (1965), p. 367.

- [20] R. Jenkins et al. “Nomenclature, symbols, units and their usage in spectrochemical analysis-VIII. Nomenclature system for X-ray spectroscopy (Recommendations 1991)”. *Pure and applied chemistry* 63.5 (1991), pp. 735–746.
- [21] T. Schoonjans et al. “A general Monte Carlo simulation of energy dispersive X-ray fluorescence spectrometers — Part 5: Polarized radiation, stratified samples, cascade effects, M-lines”. *Spectrochimica Acta Part B: Atomic Spectroscopy* 70 (2012), pp. 10–23. ISSN: 0584-8547.
- [22] L. Vincze et al. “A general Monte Carlo simulation of ED-XRF spectrometers. II: Polarized monochromatic radiation, homogeneous samples”. *Spectrochimica Acta Part B: Atomic Spectroscopy* 50.2 (1995), pp. 127–147.
- [23] R. J. Bakker. “Status and commissioning-results of BESSY II”. *Proceedings of the 1999 Particle Accelerator Conference (Cat. No. 99CH36366)*. Vol. 1. IEEE. 1999, pp. 197–199.
- [24] Helmholtz-Zentrum Berlin. *Photon Source BESSY II*. Oct. 14, 2019. URL: [https://www.helmholtz-berlin.de/media/media/zentrum/grossgeraete/bessy/hzb-infografik-bessy-2015-001\\_en\\_web.jpg](https://www.helmholtz-berlin.de/media/media/zentrum/grossgeraete/bessy/hzb-infografik-bessy-2015-001_en_web.jpg).
- [25] F. R. Elder et al. “Radiation from electrons in a synchrotron”. *Physical Review* 71.11 (1947), p. 829.
- [26] B. Holst. *Undulator*. Oct. 14, 2019. URL: <https://en.wikipedia.org/wiki/File:Undulator.png>.
- [27] W. Görner et al. “BAMline: the first hard X-ray beamline at BESSY II”. *Nuclear Instruments and Methods in Physics Research Section A: Accelerators, Spectrometers, Detectors and Associated Equipment* 467-468 (2001). 7th Int.Conf. on Synchrotron Radiation Instrumentation, pp. 703–706. ISSN: 0168-9002.
- [28] H. Riesemeier et al. “Layout and first XRF applications of the BAMline at BESSY II”. *X-Ray Spectrometry: An International Journal* 34.2 (2005), pp. 160–163.
- [29] A. Rack et al. “High resolution synchrotron-based radiography and tomography using hard X-rays at the BAMline (BESSY II)”. *Nuclear Instruments and Methods in Physics Research Section A: Accelerators, Spectrometers, Detectors and Associated Equipment* 586.2 (2008), pp. 327–344.
- [30] E. Strub et al. “Measurements with compound refractive lenses at the “BAMline””. *Nuclear Instruments and Methods in Physics Research Section B: Beam Interactions with Materials and Atoms* 266.10 (2008). Accelerators in Applied Research and Technology, pp. 2165–2168. ISSN: 0168-583X.
- [31] K. Sera. “Particle-Induced X-Ray Emission”. *Compendium of Surface and Interface Analysis*. Ed. by The Surface Science Society of Japan. Singapore: Springer Singapore, 2018, pp. 425–434. ISBN: 978-981-10-6156-1.
- [32] D. Meyer. *Die Technik der Feuervergoldung*. Oct. 18, 2019. URL: <http://feuervergoldung.eu/Technik.html>.
- [33] B. Vekemans et al. “Analysis of X-ray spectra by iterative least squares (AXIL): New developments”. *X-Ray Spectrometry* 23.6 (1994), pp. 278–285.

- [34] J. H. Hubbell and S. M. Seltzer. *Tables of X-ray mass attenuation coefficients and mass energy-absorption coefficients 1 keV to 20 MeV for elements Z= 1 to 92 and 48 additional substances of dosimetric interest*. Tech. rep. National Inst. of Standards and Technology-PL, Gaithersburg, MD (United . . ., 1995.

## Danksagung

Diese Arbeit ist meinem verstorbenen Vater gewidmet.

Mein Dank gebührt zu allererst meiner Familie und Freunden, im speziellen meiner Mutter, meinem Stiefvater, meinen Geschwistern und natürlich den beiden Familienhunden für die nötige Unterstützung und willkommenen Ablenkungen.

Für die Betreuung dieser Arbeit möchte ich ganz besonders Herr PD Dr. Erik Strub danken, der die Arbeit nicht nur ermöglichte, sondern auch fachlich und persönlich begleitete und stets für Fragen und Diskussionen offen war.

Ihm und Herrn Prof. Dr. Johannes Ermert ist zudem für die Korrektur und Abnahme der vorliegenden Arbeit zu danken.

Zudem sei dem gesamten Arbeitskreis Analytik und kernchemische Grundlagen für die tolle Arbeitsatmosphäre gedankt.



## MC Simulations Data

Shown here are the results of the MC simulations with the XMI-MSIM software. The Hg content was determined from the simulation data and compared to the actually set Hg content of the simulated layer. The difference between these two values is shown here.

Layerthick- ness [ $\mu\text{m}$ ]	Expected 0.1 Hg/(Au+Hg)			Expected 0.35 Hg/(Au+Hg)		
	Differenz (Ist-Soll) Hg/(Au+Hg)			Differenz (Ist-Soll) Hg/(Au+Hg)		
	$L_{\alpha 1}$	$L_{\alpha 2}$	$L_{\alpha 1}+L_{\alpha 2}$	$L_{\alpha 1}$	$L_{\alpha 2}$	$L_{\alpha 1}+L_{\alpha 2}$
0.1	0.0063	0.0064	0.0063	0.0154	0.0156	0.0154
1	0.0071	0.0072	0.0071	0.0166	0.0169	0.0166
3	0.0086	0.0088	0.0087	0.0197	0.0200	0.0197
10	0.0113	0.0114	0.0113	0.0255	0.0257	0.0255
20	0.0120	0.0121	0.0120	0.0267	0.0269	0.0267
100	0.0121	0.0121	0.0121	0.0271	0.0272	0.0271

Layerthick- ness [ $\mu\text{m}$ ]	Expected 0.15 Hg/(Au+Hg)			Expected 0.4 Hg/(Au+Hg)		
	Differenz (Ist-Soll) Hg/(Au+Hg)			Differenz (Ist-Soll) Hg/(Au+Hg)		
	$L_{\alpha 1}$	$L_{\alpha 2}$	$L_{\alpha 1}+L_{\alpha 2}$	$L_{\alpha 1}$	$L_{\alpha 2}$	$L_{\alpha 1}+L_{\alpha 2}$
0.1	0.0088	0.0090	0.0088	0.0162	-0.0028	0.0143
1	0.0099	0.0100	0.0099	0.0172	0.0175	0.0172
3	0.0120	0.0122	0.0120	0.0204	0.0207	0.0204
10	0.0158	0.0159	0.0158	0.0262	0.0264	0.0262
20	0.0165	0.0166	0.0165	0.0274	0.0276	0.0274
100	0.0167	0.0168	0.0168	0.0275	0.0277	0.0275

Layerthick- ness [ $\mu\text{m}$ ]	Expected 0.2 Hg/(Au+Hg)			Expected 0.45 Hg/(Au+Hg)		
	Differenz (Ist-Soll) Hg/(Au+Hg)			Differenz (Ist-Soll) Hg/(Au+Hg)		
	$L_{\alpha 1}$	$L_{\alpha 2}$	$L_{\alpha 1}+L_{\alpha 2}$	$L_{\alpha 1}$	$L_{\alpha 2}$	$L_{\alpha 1}+L_{\alpha 2}$
0.1	0.0110	0.0112	0.0110	0.0166	0.0168	0.0166
1	0.0122	0.0124	0.0122	0.0176	0.0178	0.0176
3	0.0148	0.0150	0.0148	0.0206	-0.3683	-0.1323
10	0.0193	0.0195	0.0193	0.0261	0.0264	0.0261
20	0.0203	0.0204	0.0203	0.0277	0.0279	0.0277
100	0.0205	0.0206	0.0205	0.0277	0.0279	0.0277

Layerthick- ness [ $\mu\text{m}$ ]	Expected 0.25 Hg/(Au+Hg)			Expected 0.5 Hg/(Au+Hg)		
	Differenz (Ist-Soll) Hg/(Au+Hg)			Differenz (Ist-Soll) Hg/(Au+Hg)		
	$L_{\alpha 1}$	$L_{\alpha 2}$	$L_{\alpha 1}+L_{\alpha 2}$	$L_{\alpha 1}$	$L_{\alpha 2}$	$L_{\alpha 1}+L_{\alpha 2}$
0.1	0.0128	0.0130	0.0129	0.0163	0.0165	0.0163
1	0.0141	0.0143	0.0141	0.0175	0.0177	0.0175
3	0.0169	0.0172	0.0170	0.0202	0.0206	0.0203
10	0.0220	0.0223	0.0221	0.0257	0.0260	0.0257
20	0.0232	0.0234	0.0233	0.0271	0.0273	0.0271
100	0.0235	0.0236	0.0235	0.0270	0.0271	0.0270

Layerthick- ness [ $\mu\text{m}$ ]	Expected 0.3 Hg/(Au+Hg)		
	Differenz (Ist-Soll) Hg/(Au+Hg)		
	$L_{\alpha 1}$	$L_{\alpha 2}$	$L_{\alpha 1}+L_{\alpha 2}$
0.1	0.0143	0.0145	0.0143
1	0.0156	0.0159	0.0156
3	0.0186	0.0189	0.0186
10	0.0242	0.0244	0.0242
20	0.0254	0.0255	0.0254
100	0.0257	0.0258	0.0257

**Figure 30** – Simulation data for the XMI-MSIM calculation. The tables show the determined differences between the Hg content of the simulated layer (Soll) and the Hg content as determined from the line comparison (Ist) for the comparison of different lines ( $L_{\alpha 1,1}$ ,  $L_{\alpha 1,1}$  and  $L_{\alpha 1,1}+L_{\alpha 1,2}$ ) for different layer thicknesses.

## Polished vs. Unpolished

Shown here are the line intensities as determined with the AXIL code from the XRF spectra for the Cu, Au, and Hg lines. From these intensities, the Hg content was determined, the average calculated and standard deviation determined.

Probe	Cu	Au	Hg	Hg/(Au+Hg)		sample	Cu	Au	Hg	Hg/(Au+Hg)
c3 polished	176760	14531	1800	0.110219827		SD1 polished --> unpolished	179	37770	8002	0.174823036
c3 polished	187677	11632	1343	0.103506744		SD1 polished --> unpolished	135	36711	6773	0.15575844
c3 polished	177797	14733	1719	0.104485777		SD1 polished --> unpolished	214	31545	7794	0.198123999
c3 polished	179974	14109	1685	0.106686083		SD1 polished --> unpolished	81	30666	9861	0.243319269
c3 polished	193521	10194	1159	0.102087554		SD1 polished --> unpolished	66	39393	7422	0.15853893
c3 polished	192795	10720	1120	0.094594595		SD1 polished --> unpolished	62	35085	8569	0.196293581
			<b>Average</b>	0.103596763	0.005244503	SD1 polished --> unpolished	95	47314	7513	0.137031025
c3 unpolished	151732	20214	2667	0.116559591		SD1 polished --> unpolished	130	40335	9102	0.184113114
c3 unpolished	162913	18647	2413	0.114577398		SD1 polished --> unpolished	103	45233	8261	0.154428534
c3 unpolished	139591	23496	3043	0.114661442		SD1 polished --> unpolished	81	41030	8843	0.177310368
c3 unpolished	174165	15076	1836	0.108561968		SD1 polished --> unpolished	135	48965	7526	0.133224761
c3 unpolished	145426	23366	3182	0.11985837		SD1 polished --> unpolished	100	41375	8808	0.175517606
c3 unpolished	172331	15493	1861	0.107237524		SD1 polished --> unpolished	139	43375	8763	0.16807319
			<b>Average</b>	0.113576049	0.004813891	SD1 polished --> unpolished	183	44966	9314	0.171591746
						SD1 polished --> unpolished	139	40919	9393	0.186695023
						SD1 polished --> unpolished	142	40506	7874	0.162753204
Probe	Cu	Au	Hg	Hg/(Au+Hg)		sample	Cu	Au	Hg	Hg/(Au+Hg)
c5 polished	140319	21114	4675	0.18127884						
c5 polished	155872	18033	3883	0.177176492						
c5 polished	144769	21768	4829	0.18156183		SE1 polished --> unpolished	96	57540	19789	0.255906581
c5 polished	146446	20271	4181	0.170988058		SE1 polished --> unpolished	153	60518	20614	0.254079771
c5 polished	143311	21992	4772	0.178299208		SE1 polished --> unpolished	148	57294	20062	0.259346398
c5 polished	156289	18568	4115	0.181413393		SE1 polished --> unpolished	94	51895	19622	0.274368332
			<b>Average</b>	0.17845297	0.004093717	SE1 polished --> unpolished	69	49659	18097	0.267090737
c5 unpolished	142838	22210	4923	0.181439575		SE1 polished --> unpolished	70	42132	16960	0.287010086
c5 unpolished	144628	20046	4423	0.180759328		SE1 polished --> unpolished	110	43816	17461	0.28495194
c5 unpolished	157044	18628	4089	0.179997359		SE1 polished --> unpolished	88	40254	16330	0.288597483
c5 unpolished	139586	22555	5066	0.183411173		SE1 polished --> unpolished	113	41048	16081	0.28148576
c5 unpolished	155480	18414	4027	0.179448331		SE1 polished --> unpolished	76	37985	15207	0.285888855
c5 unpolished	141395	21893	4837	0.180957725		SE1 polished --> unpolished	275	41492	16623	0.286036307
			<b>Average</b>	0.181002249	0.001376926	SE1 polished --> unpolished	110	41748	15992	0.276965708
						SE1 polished --> unpolished	100	38024	14898	0.281508635
						SE1 polished --> unpolished	668	36694	16414	0.309068314
Probe	Cu	Au	Hg	Hg/(Au+Hg)		sample	Cu	Au	Hg	Hg/(Au+Hg)
c1 polished	125018	25187	5744	0.185703663		SE1 polished --> unpolished	162	38087	14986	0.282365798
c1 polished	116928	26126	6098	0.189237835		SE1 polished --> unpolished	53	35526	14408	0.288540874
c1 polished	130888	22786	5127	0.183677856						
c1 polished	129708	22098	4904	0.181616177						
c1 polished	120555	25213	5768	0.186178626						
c1 polished	137112	22005	4716	0.176490401						
			<b>Average</b>	0.183817426	0.004406002	SE2 polished --> unpolished	79	53366	14478	0.207290533
c1 unpolished	98775	28634	6501	0.185029173		SE2 polished --> unpolished	156	52191	14383	0.216045303
c1 unpolished	114248	26602	6025	0.184663009		SE2 polished --> unpolished	142	53908	14233	0.208875714
c1 unpolished	108955	27846	6162	0.181192661		SE2 polished --> unpolished	100	52860	14582	0.216215415
c1 unpolished	97422	28802	6404	0.181900812		SE2 polished --> unpolished	104	51850	15325	0.228135467
c1 unpolished	104025	28739	6350	0.180968395		SE2 polished --> unpolished	65	47879	14175	0.228430077
c1 unpolished	104758	28738	6390	0.181906172		SE2 polished --> unpolished	113	43140	13502	0.238374351
			<b>Average</b>	0.182610037	0.00177591	SE2 polished --> unpolished	139	55299	13739	0.199006344
						SE2 polished --> unpolished	107	50130	13172	0.208081893
						SE2 polished --> unpolished	72	49670	12341	0.199013078
						SE2 polished --> unpolished	86	41232	11017	0.21085571
						SE2 polished --> unpolished	93	41045	11857	0.224131413
						SE2 polished --> unpolished	63	35785	11473	0.24277371
						SE2 polished --> unpolished	91	35482	10634	0.230592419
						SE2 polished --> unpolished	65	42912	10403	0.195123324
						SE2 polished --> unpolished	114	43938	11095	0.201606309

**Figure 31** – Line intensity data for the Cu, Au, and Hg lines of the polished vs. unpolished measurements with Cu samples on the left and Ag samples on the right. Given are the line intensities for Cu, Au, Hg L lines as determined with the AXIL code, the Hg content calculated from the intensities, as well as the average and standard deviation for Cu samples on the polished and unpolished side.

## Temperature Profile

The following figure compares the single line scans over comparison samples for amalgamized and not-amalgamized Cu substrates to the amalgamized Cu substrate mapping sample. The aim was to verify a similar structure in the Hg content development.

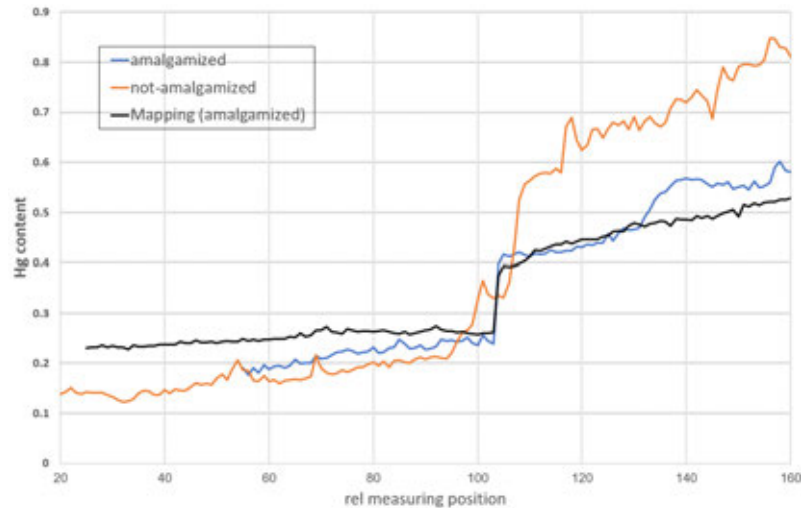


**Figure 32** – Comparison between the Hg content of temperature profile samples of not-amalgamized and amalgamized Cu substrates. Aim of this was to see if amalgamation influences the general structure of the Hg content in a temperature profile. This does not seem to be the case.

## Artificial Aging

This section shows the measurement data for artificial aging analysis during this thesis.

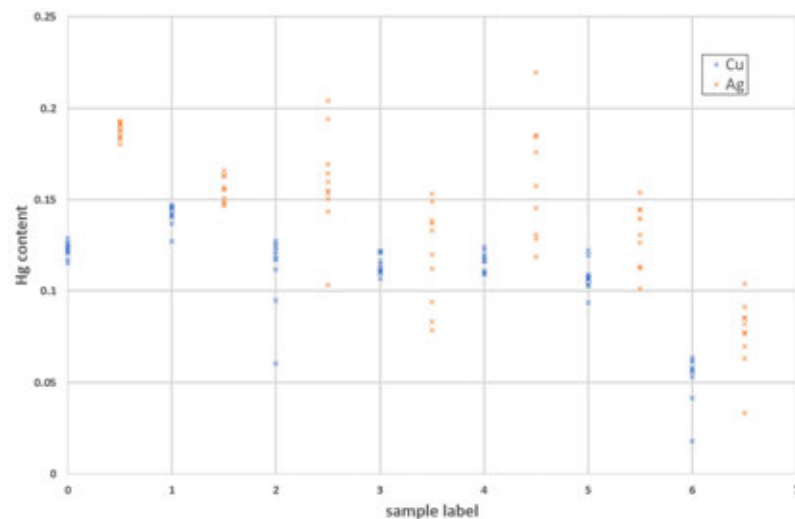


**Figure 33** – The figure shows all Hg contents determined during the preliminary artificial aging test run. Ag samples are off-set to the right for readability, the sample label is the same as for the Cu samples to the left. An overview over the details of the different samples is given in table 6.

Probe	Hg content	Probe	Hg content	Probe	Hg content	Probe	Hg content	Probe	Hg content	Probe	Hg content						
180°C	0d	0.156869	190°C	0d	0.202678	200°C	0d	0.1476425	180°C	3d	0.099183	190°C	3d	0.063108	200°C	3d	0.0604
180°C	0d	0.157706	190°C	0d	0.205859	200°C	0d	0.1549553	180°C	3d	0.105892	190°C	3d	0.111847	200°C	3d	0.073136
180°C	0d	0.137623	190°C	0d	0.214812	200°C	0d	0.1559218	180°C	3d	0.094296	190°C	3d	0.114899	200°C	3d	0.063633
180°C	0d	0.154168	190°C	0d	0.238348	200°C	0d	0.1467301	180°C	3d	0.104821	190°C	3d	0.121247	200°C	3d	0.060438
180°C	0d	0.152708	190°C	0d	0.24212	200°C	0d	0.1580717	180°C	3d	0.098905	190°C	3d	0.121592	200°C	3d	0.058935
180°C	0d	0.137448	190°C	0d	0.243874	200°C	0d	0.1488913	180°C	3d	0.108505	190°C	3d	0.132914	200°C	3d	0.061401
180°C	0d	0.142162	190°C	0d	0.234845	200°C	0d	0.1498921	180°C	3d	0.104536	190°C	3d	0.114316	200°C	3d	0.066283
180°C	0d	0.143238	190°C	0d	0.238792	200°C	0d	0.1586224	180°C	3d	0.104094	190°C	3d	0.112487	200°C	3d	0.061149
180°C	0d	0.152307	190°C	0d	0.215886	200°C	0d	0.1466182	180°C	3d	0.116839	190°C	3d	0.11881	200°C	3d	0.079742
180°C	0d	0.163156	190°C	0d	0.204333	200°C	0.25d	0.1003476	180°C	3d	0.070897	190°C	3d	0.117345	200°C	3d	0.063926
180°C	0d	0.16828	190°C	0d	0.173096	200°C	0.25d	0.0935078	180°C	3d	0.066567	190°C	3d	0.161007	200°C	3d	0.064772
180°C	0d	0.16003	190°C	0d	0.141442	200°C	0.25d	0.1051424	180°C	3d	0.077868	190°C	3d	0.11306	200°C	3d	0.062178
180°C	0d	0.166805	190°C	0d	0.232705	200°C	0.25d	0.0965943	180°C	3d	0.068636	190°C	3d	0.134618	200°C	3d	0.066155
180°C	0d	0.170638	190°C	0d	0.135556	200°C	0.25d	0.0985284	180°C	3d	0.071845	190°C	3d	0.131027	200°C	3d	0.067362
180°C	0d	0.173939	190°C	0d	0.146411	200°C	0.25d	0.1005863	180°C	3d	0.078752	190°C	3d	0.125094	200°C	3d	0.064943
180°C	0d	0.169664	190°C	0d	0.129904	200°C	0.25d	0.102705	180°C	3d	0.079373	190°C	3d	0.108954	200°C	3d	0.094314
180°C	0d	0.180711	190°C	0d	0.129584	200°C	0.25d	0.1012222	180°C	3d	0.075659	190°C	3d	0.109496	200°C	3d	0.086238
180°C	0d	0.162839	190°C	0d	0.128741	200°C	0.25d	0.1029174	180°C	3d	0.09885	190°C	3d	0.126514	200°C	3d	0.084022
180°C	0d	0.173141	190°C	0d	0.172265	200°C	0.25d	0.099501	180°C	3d	0.098669	190°C	3d	0.114705	200°C	3d	0.056333
180°C	0d	0.173284	190°C	0d	0.211038	200°C	0.25d	0.1188695	180°C	3d	0.101559	190°C	3d	0.126212	200°C	3d	0.062372
180°C	0d	0.181041	190°C	0d	0.185004	200°C	0.25d	0.1021365	180°C	3d	0.106025	190°C	3d	0.128758	200°C	3d	0.060692
180°C	0d	0.171222	190°C	0d	0.176221	200°C	0.25d	0.104713	180°C	3d	0.09827	190°C	3d	0.128285	200°C	3d	0.064105
180°C	0d	0.187843	190°C	0d	0.182462	200°C	0.25d	0.1134438	180°C	3d	0.093686	190°C	3d	0.130574	200°C	3d	0.061013
180°C	0d	0.174689	190°C	0d	0.174368	200°C	0.25d	0.115959	180°C	3d	0.115562	190°C	3d	0.127568	200°C	3d	0.063645
180°C	0d	0.172621	190°C	0d	0.176607	200°C	0.25d	0.0967613	180°C	3d	0.099349	190°C	3d	0.104602	200°C	3d	0.065078
180°C	0d	0.166526	190°C	0d	0.17036	200°C	0.25d	0.1065036	180°C	3d	0.094881	190°C	3d	0.131815	200°C	3d	0.064267
180°C	0d	0.176246	190°C	0d	0.134578	200°C	0.25d	0.1107529	180°C	3d	0.081431	190°C	3d	0.117858	200°C	3d	0.070338
180°C	0.25d	0.126832	190°C	0.25d	0.143277	200°C	0.25d	0.1114545	180°C	7d	0.100454	190°C	7d	0.106129	200°C	7d	0.060673
180°C	0.25d	0.123168	190°C	0.25d	0.137877	200°C	0.25d	0.1119494	180°C	7d	0.094239	190°C	7d	0.122779	200°C	7d	0.068973
180°C	0.25d	0.124746	190°C	0.25d	0.150875	200°C	0.25d	0.1007836	180°C	7d	0.081388	190°C	7d	0.109359	200°C	7d	0.073746
180°C	0.25d	0.129853	190°C	0.25d	0.137644	200°C	0.25d	0.1030695	180°C	7d	0.09283	190°C	7d	0.103637	200°C	7d	0.05245
180°C	0.25d	0.141739	190°C	0.25d	0.142275	200°C	0.25d	0.1042427	180°C	7d	0.095305	190°C	7d	0.101551	200°C	7d	0.053723
180°C	0.25d	0.133374	190°C	0.25d	0.147952	200°C	0.25d	0.1153593	180°C	7d	0.073067	190°C	7d	0.126363	200°C	7d	0.051908
180°C	0.25d	0.123215	190°C	0.25d	0.133257	200°C	0.25d	0.100072	180°C	7d	0.073571	190°C	7d	0.101067	200°C	7d	0.054521
180°C	0.25d	0.137509	190°C	0.25d	0.134616	200°C	0.25d	0.1181344	180°C	7d	0.098466	190°C	7d	0.104347	200°C	7d	0.059058
180°C	0.25d	0.125352	190°C	0.25d	0.134076	200°C	0.25d	0.1197982	180°C	7d	0.08089	190°C	7d	0.089811	200°C	7d	0.053472
180°C	0.25d	0.139976	190°C	0.25d	0.144236	200°C	1d	0.0944036	180°C	7d	0.080741	190°C	7d	0.089763	200°C	7d	0.085489
180°C	0.25d	0.099891	190°C	0.25d	0.112695	200°C	1d	0.1148187	180°C	7d	0.075458	190°C	7d	0.107162	200°C	7d	0.082248
180°C	0.25d	0.112498	190°C	0.25d	0.098119	200°C	1d	0.092747	180°C	7d	0.08689	190°C	7d	0.110159	200°C	7d	0.087043
180°C	0.25d	0.137701	190°C	0.25d	0.115309	200°C	1d	0.083141	180°C	7d	0.090114	190°C	7d	0.091293	200°C	7d	0.058299
180°C	0.25d	0.106029	190°C	0.25d	0.137004	200°C	1d	0.0995425	180°C	7d	0.094694	190°C	7d	0.108866	200°C	7d	0.090653
180°C	0.25d	0.111508	190°C	0.25d	0.109811	200°C	1d	0.1032088	180°C	7d	0.103687	190°C	7d	0.096939	200°C	7d	0.089077
180°C	0.25d	0.111133	190°C	0.25d	0.162067	200°C	1d	0.0843487	180°C	7d	0.100894	190°C	7d	0.106908	200°C	7d	0.045982
180°C	0.25d	0.130393	190°C	0.25d	0.138876	200°C	1d	0.0930029	180°C	7d	0.091512	190°C	7d	0.099184	200°C	7d	0.073321
180°C	0.25d	0.108015	190°C	0.25d	0.128269	200°C	1d	0.0886225	180°C	7d	0.114729	190°C	7d	0.112529	200°C	7d	0.078779
180°C	0.25d	0.092616	190°C	0.25d	0.146556	200°C	1d	0.0709172	180°C	7d	0.077896	190°C	7d	0.123053	200°C	7d	0.049184
180°C	0.25d	0.091574	190°C	0.25d	0.144814	200°C	1d	0.0731645	180°C	7d	0.082917	190°C	7d	0.118796	200°C	7d	0.04477
180°C	0.25d	0.113232	190°C	0.25d	0.140643	200°C	1d	0.0724489	180°C	7d	0.080159	190°C	7d	0.107213	200°C	7d	0.073123
180°C	0.25d	0.090489	190°C	0.25d	0.143807	200°C	1d	0.0790458	180°C	7d	0.075121	190°C	7d	0.124413	200°C	7d	0.042168
180°C	0.25d	0.091781	190°C	0.25d	0.14331	200°C	1d	0.0823788	180°C	7d	0.088836	190°C	7d	0.121622	200°C	7d	0.049928
180°C	0.25d	0.094206	190°C	0.25d	0.147565	200°C	1d	0.0772187	180°C	7d	0.081273	190°C	7d	0.112901	200°C	7d	0.052093
180°C	0.25d	0.089688	190°C	0.25d	0.123562	200°C	1d	0.0771733	180°C	7d	0.072603	190°C	7d	0.118129	200°C	7d	0.067755
180°C	0.25d	0.096347	190°C	0.25d	0.156187	200°C	1d	0.0850351	180°C	7d	0.102845	190°C	7d	0.115169	200°C	7d	0.049703
180°C	0.25d	0.093238	190°C	0.25d	0.138172	200°C	1d	0.0812018	180°C	7d	0.07794	190°C	7d	0.122777	200°C	7d	0.056243
180°C	1d	0.119979	190°C	1d	0.120352	200°C	1d	0.0882353	180°C	10d	0.111493	190°C	10d	0.102641	200°C	10d	0.068226
180°C	1d	0.123016	190°C	1d	0.104829	200°C	1d	0.0851351	180°C	10d	0.084927	190°C	10d	0.126876	200°C	10d	0.046351
180°C	1d	0.117787	190°C	1d	0.114327	200°C	1d	0.0888003	180°C	10d	0.103476	190°C	10d	0.115872	200°C	10d	0.084707
180°C	1d	0.114547	190°C	1d	0.117257	200°C	1d	0.0780553	180°C	10d	0.11213	190°C	10d	0.115095	200°C	10d	0.076321
180°C	1d	0.118156	190°C	1d	0.138338	200°C	1d	0.0906579	180°C	10d	0.109555	190°C	10d	0.120742	200°C	10d	0.059426
180°C	1d	0.115727	190°C	1d	0.128456	200°C	1d	0.0899173	180°C	10d	0.108909	190°C	10d	0.159133	200°C	10d	0.083554
180°C	1d	0.119617	190°C	1d	0.122619	200°C	1d	0.0775699	180°C	10d	0.103893	190°C	10d	0.112551	200°C	10d	0.067755
180°C	1d	0.127531	190°C	1d	0.118809	200°C	1d	0.0778535	180°C	10d	0.11772	190°C	10d	0.099744	200°C	10d	0.077114
180°C	1d	0.119581	190°C	1d	0.120734	200°C	1d	0.0880393	180°C	10d	0.062912	190°C	10d	0.121335	200°C	10d	0.077119
180°C	1d	0.132149	190°C	1d	0.102696	200°C	1d	0.0886444	180°C	10d	0.090441	190°C	10d	0.086444	200°C	10d	0.074491
180°C	1d	0.111062	190°C	1d	0.118361	200°C	1d	0.085389	180°C	10d	0.085389	190°C	10d	0.098868	200°C	10d	0.070135
180°C	1d	0.1314	190°C	1d	0.123596	200°C	1d	0.075189	180°C	10d	0.075189	190°C	10d	0.085019	200°C	10d	0.062915
180°C	1d	0.148067	190°C	1d	0.117808	200°C	1d	0.114814	180°C	10d	0.114814	190°C					

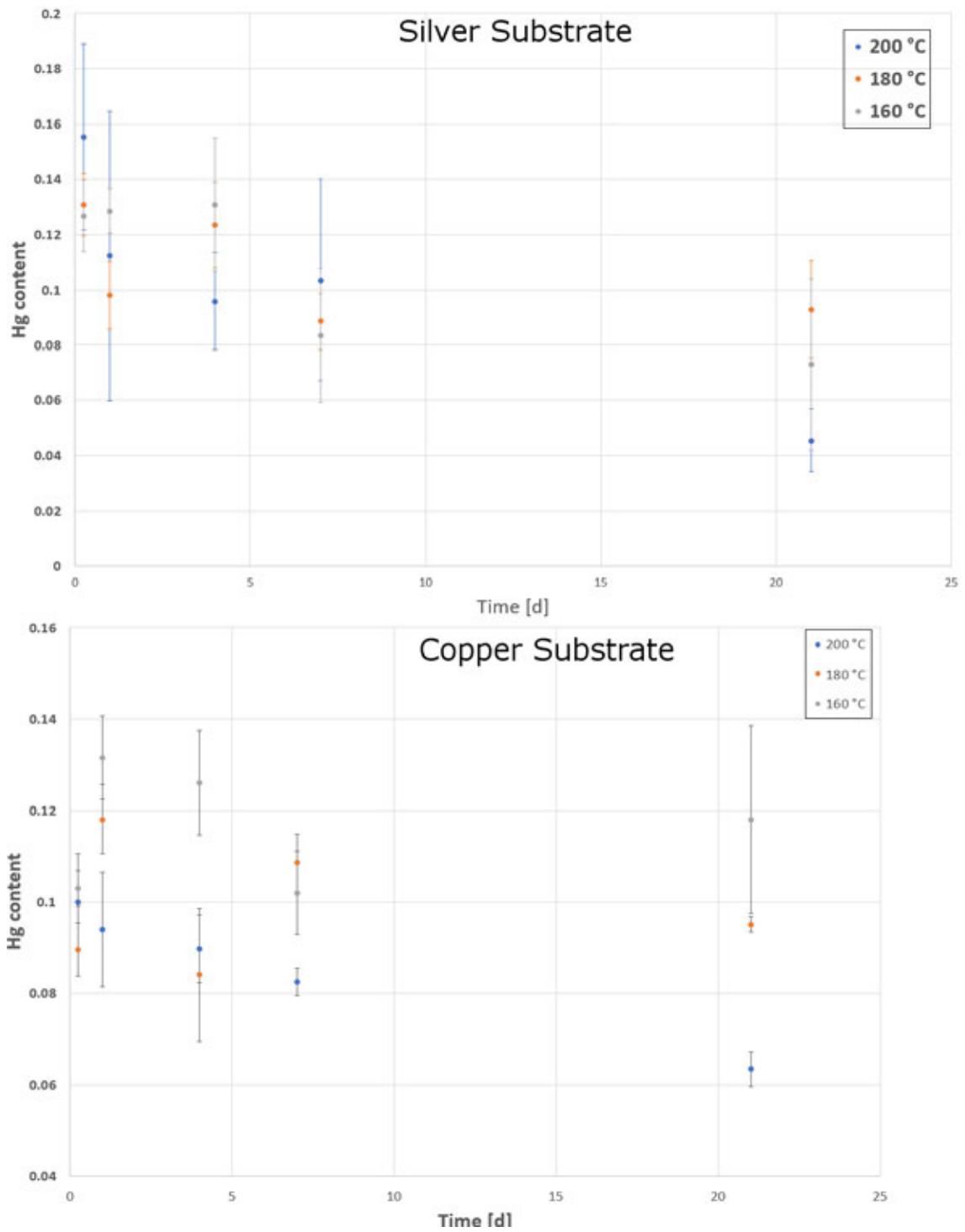


**Figure 35** – Hg contents as determined from a second structured artificial aging run of fire gilded Ag and Cu substrates. The results are very inconclusive due to the low number of measurements performed to acquire this data.

## Cross Section Analysis

This section shows measurement data of cross section analysis of fire gilded Ag and Cu substrates in various forms.

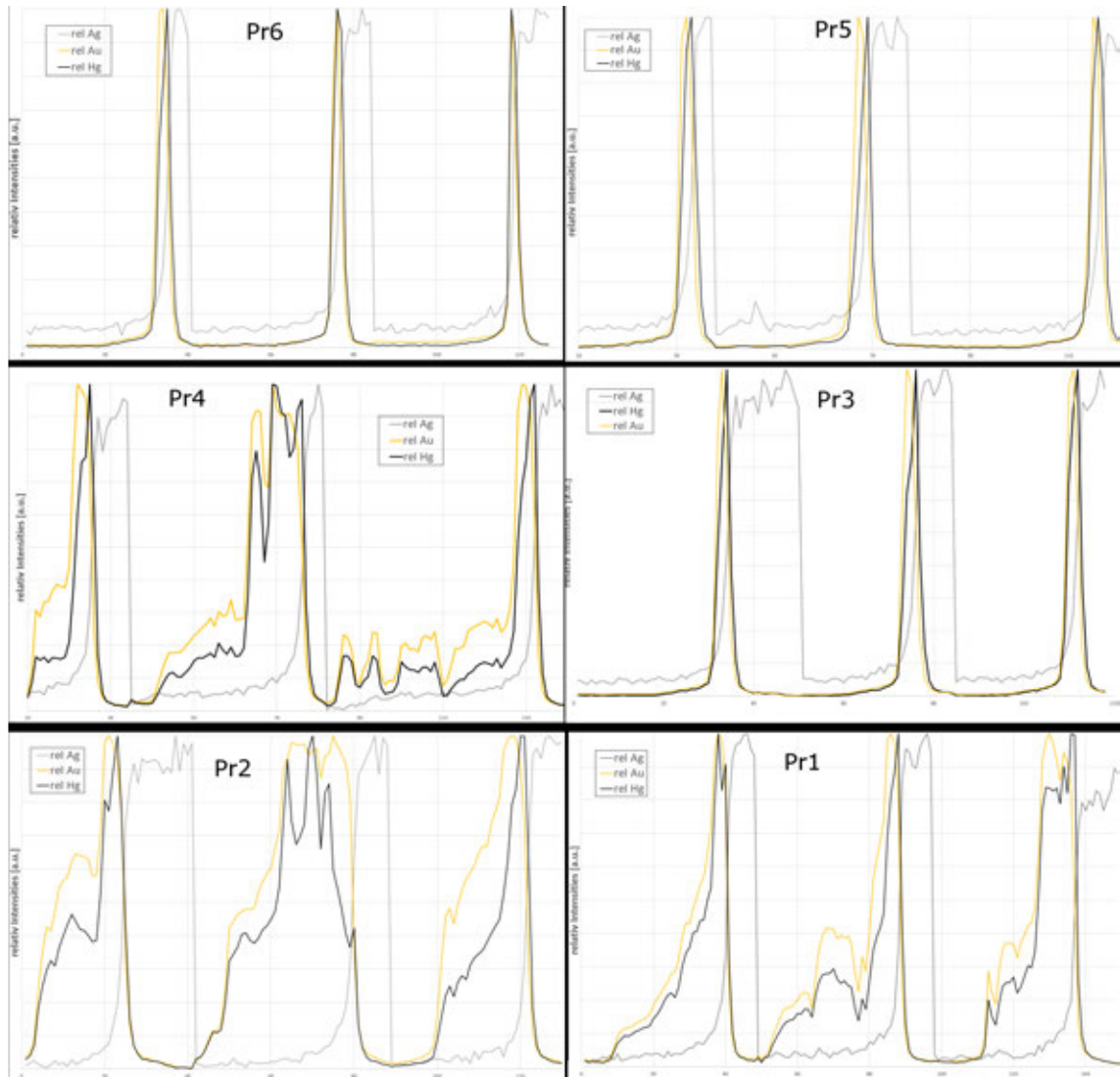


**Figure 36** – Measurement data for cross section analysis of six different fire gilded Ag substrates. Formatted to show the general trend of Hg enrichment at the interface. The figure consists of six graphs, one for each sample. Each graph shows the relative intensities of Ag, Au, and Hg of three different line scans across the cross section. Relative values are the ratio of a measured intensity vs the highest measured intensity of the respective element during the line scan. Through this, the relative information between Au and Hg intensities is lost. Instead the emphasis is on the possible observation of a Hg enrichment. If Hg and Au peak at different positions the Hg content will not be constant from surface to substrate.

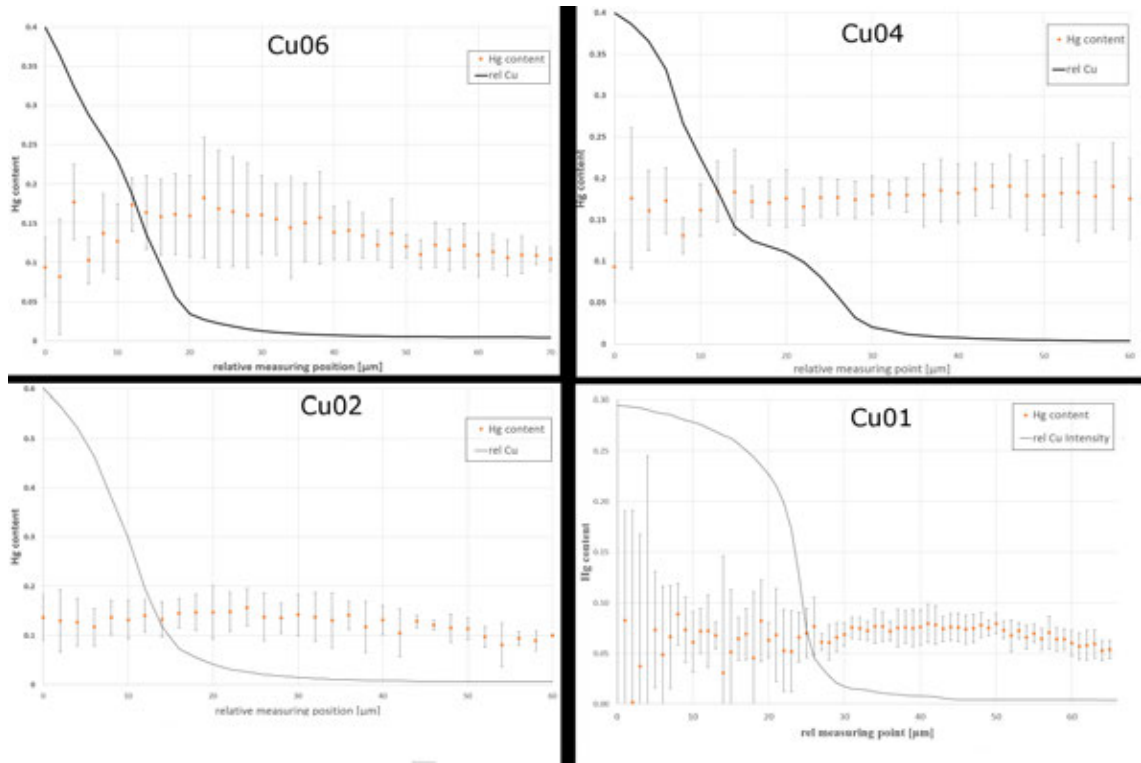


**Figure 37** – Hg content depth profile of four Cu samples, determined with 4 cross section line scans each. Surface on the right, substrate on the left. Uncertainties are the standard deviations from the average.

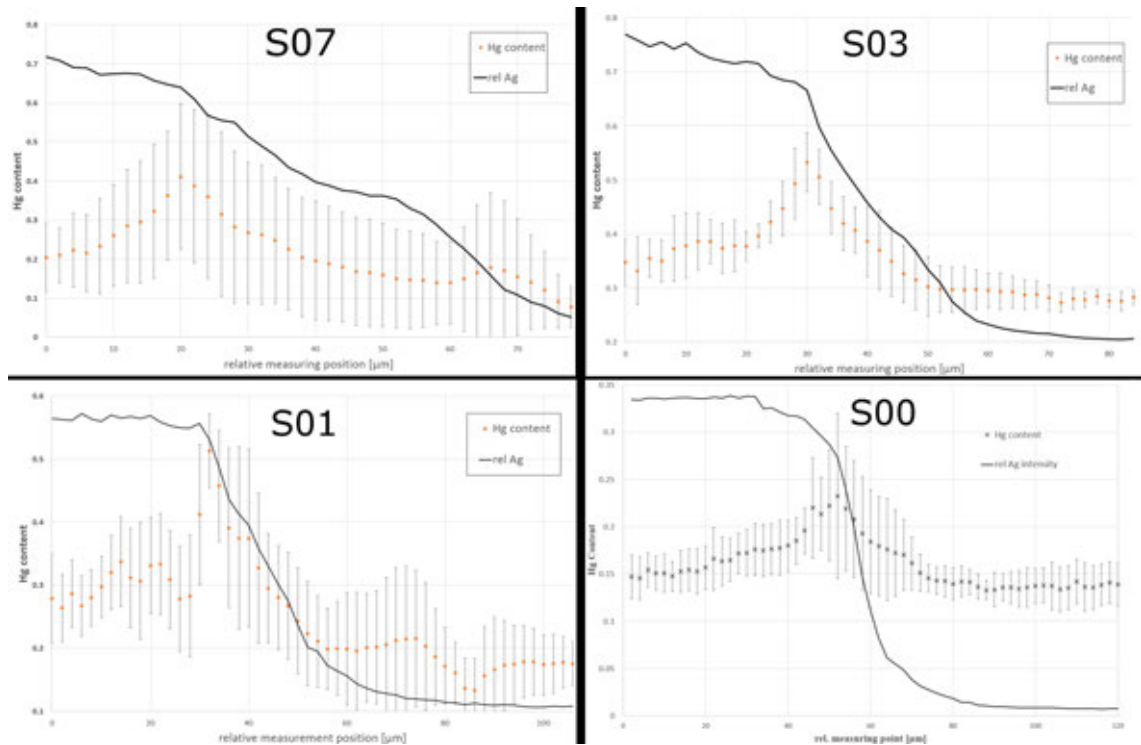


**Figure 38** – Hg content depth profile of four Ag samples, determined with 4 cross section line scans each. Surface on the right, substrate on the left. Uncertainties are the standard deviations from the average.